International Journal of Multiphase Flow 160 (2023) 104379

Contents lists available at ScienceDirect

International Journal of Multiphase Flow

journal homepage: www.elsevier.com/locate/ijmulflow

Drafting, Kissing and Tumbling Process of Two Particles: The Effect of Morphology

Xiaoming Zhang [a], Pejman Tahmasebi [b,*]

[a] College of Engineering and Applied Science, University of Wyoming, Laramie, WY 82071, USA
[b] Colorado School of Mines, Golden, CO 80401, USA

ABSTRACT

The gravity-driven sedimentation of particles in viscous fluids can be found in many applications. This problem has been studied for spherical or other well-defined shapes while the actual morphology of particles is ignored. However, it has been shown experimentally and numerically that the particle shape plays an important role in granular motion. This problem is generally described by the drafting-kissing-tumbling (DKT) phenomenon which is associated with the settling of particle pairs. In this paper, we numerically investigate the DKT process of irregular particles by coupling the mechanical and hydromechanical effects. Here, 16 irregular particles with different sphericity and roundness, including a spherical particle, are selected to study the effect of particle shape in the DKT process. Moreover, four orientations for each irregular particle are considered, which results in 65 sedimentation models. Our results show that particles with low sphericity are more sensitive to orientation because low sphericity particles tend to adjust the orientation and keep the broad side perpendicular to the fluid streamline direction. On the other hand, lower roundness accelerates the happening of the tumbling stage and makes the separation of particle pairs faster. Furthermore, the comparison of the vertical velocity shows that it decreases when roundness or sphericity is smaller.

1. Introduction

Particle motion in granular systems is ubiquitous in nature, such as landslides, collapse, debris flows, and solid deformation in porous media, as well as in modern industries of chemical, pharmaceutics, mining, food processing, and cosmetics (Cleary, 2000; Fries et al., 2011; Katz et al., 2014; Li et al., 2004; Zhang and Tahmasebi, 2019, 2018; Davydzenka et al., 2020a, 2020b; Tahmasebi and Kamrava, 2019). One of the fundamental particle motions is the gravity-driven sedimentation of particles in a viscous fluid, in which the particle pairs undergo the drafting, kissing, and tumbling (DKT) process. Fortes et al. conducted the experiments of spherical particles falling in the water and observed the DKT scenario(Fortes et al., 1987). They described the DKT process as rearrangement mechanisms in which one sphere was captured in the wake of the other. Due to the massively unstable streamwise alignment, the two particles tumbled into a more stable cross-stream. In the *drafting* stage, more specifically, the upper particle (i.e., trailing particle) is approaching the lower particle (i.e., leading particle) due to the low pressure in the wake of the lower particle. The decrease in the distance between the two particles eventually leads the particles to touch each other, which is called *kissing*. The alignment of the two particles in the vertical direction is unstable which means the particles cannot stay one behind the other. The motion enters the *tumbling* stage where the trailing particle will gradually push the leading particle aside and take the lead and the separation of the two particles will happen eventually. The sedimentation mechanism in the DKT phenomenon reveals that two particles on the same streamlines tend to be located side by side across streamlines in a viscous fluid.

Along with experimental studies on the DKT (Dash and Lee, 2015; Fortes et al., 1987; Lomholt et al., 2002), different numerical methods have also been developed to allow one to examine various boundary conditions and other physical factors. Hu et al. developed a simulation for unsteady two-dimensional solid-liquid flows with Navier-Stokes equations solved for liquid by a finite-element formulation and Newton's equations of motion for solid particles by an Explicit-Implicit scheme (Hu et al., 1992). In this scheme, the explicitly updated particle positions lead to re-mesh the computational domain in which the Navier-Stokes equations for liquid and the implicitly discretized Newton's equations for particle velocities are solved iteratively. They numerically reproduced the DKT scenario and revealed that vortex shedding on the particle motion resulted in the rearrangement of the two particles. Ritz et al. developed a numerical continuous model for fluid-particle motion based on the governing equations of two immiscible fluids (Ritz and Caltagirone, 1999). The main characteristic of their model was to assume the solid phase to be a fluid phase with a very high viscosity whose behavior can be assimilated to that of pseudo-rigid

---

* Corresponding author.
E-mail address: tahmasebi@mines.edu (P. Tahmasebi).

https://doi.org/10.1016/j.ijmultiphaseflow.2023.104379
Received 15 March 2022; Received in revised form 13 October 2022; Accepted 2 January 2023

particles. Qi developed a lattice-Boltzmann method to simulate the sedimentation of both spherical and rectangular particles in finite-Reynolds-number flows (Qi, 1999). They reproduced the DKT process for two-dimensional circular and rectangular particles and three-dimensional spherical particles. Glowinski et al. proposed a Distributed Lagrange-Multiplier (DLM) based fictitious-domain method for the direct numerical simulation of particulate flow in a viscous incompressible fluid (Glowinski et al., 1999). This method treated the fluid-particle motion implicitly via a combined weak Navier-Stokes formulation which can cancel the mutual fluid-particle forces. A distributed Lagrange multiplier (DLM) was needed to constrain the flow inside and on each particle boundary to be a rigid-body motion. Later, Patankar et al. and Yu et al. improved the Lagrange-multiplier based fictitious-domain method to be more compatible for fluid-particle flow (Patankar et al., 2000; Yu et al., 2006). Seyed-Ahmadi and Wachs studied the particle-resolved direct numerical simulations of mono-disperse settling suspensions of cubes and spheres with different Galileo numbers and solid volume fractions. They found that cube suspensions are more homogeneous compared to sphere suspensions in all cases, which was the result of the higher angular velocities and the resulting orientation- and rotation-induced lift forces (Seyed-Ahmadi and Wachs, 2021).

Numerical simulations for fluid-particle flow make it convenient for studying the factors affecting the sedimentation process of two particles. For example, Shao et al. numerically investigated the effect of particle size on the DKT process by the DLM/Fictitious Domain Method (Xue-ming et al., 2005). Their results indicated that the two particles (smaller being the leading particle) would undergo a repeated DKT process with a small diameter ratio. They also found that smaller diameter ratios would enhance the frequency of DKT. Wang et al. numerically investigated the effect of the longitudinal distance and diameter ratio between two particles on the drafting, kissing, and tumbling (DKT) phenomenon by the lattice Boltzmann equation with a multiple-relaxation-time collision model (Wang et al., 2014). They considered three cases: two identical particles in Case-0, the larger particle being the upper in Case-1, and the smaller particle being the upper in Case-2. They found that the large initial longitudinal distance would prevent the DKT process in Case-2 while there was always a DKT process in Case-1. Ardekani et al. simulated the sedimentation of spheroidal particles by the Immersed Boundary Method (Ardekani et al., 2016). Their results indicated that the two spheroidal particles are more promptly attracted in the horizontal direction and have a larger collision distance in the DKT process. Ghosh et al. studied the DKT process between two particles of different sizes and densities in 2D by Immersed Boundary (IB) method (Ghosh and Kumar, 2020) by considering two sizes for the trailing particle. Moreover, the densities of the two particles were different in the two scenarios. They found that both the size and the density of the particles greatly affect the DKT behavior such that the key to ensuring one complete cycle of DKT is that the larger particle should have a higher density. When the larger particle has a higher density, the particles would undergo the DKT process regardless of the diameter ratio and density difference between the two particles. When the larger particle has less density, the complete DKT process is restricted to a certain diameter ratio and density difference.

To date, more efforts have been made to study the effect of particle size and density than particle shape. Many experimental and computational pieces of research have indicated that particle shape has a great influence on the motion of granular systems, such as the shear strength, angle of repose, angle of internal friction, particle stability within granular shear zones, … (Anthony and Marone, 2005; Azéma et al., 2012; Cho et al., 2006; Kawamoto et al., 2016; Robinson and Friedman, 2002; Shinohara et al., 2000). In this paper, therefore, we aim to investigate the effect of grains' morphology on the sedimentation process of two particles by considering a systematic variation of the sphericity and roundness in a set of complex particles. This allows us to study how a gradual change of the morphology quantified using two important descriptors can affect the DKT behaviors. The sedimentation simulations of the irregular particles are achieved by coupling the Computational Fluid Dynamics (CFD) with a novel image-based Discrete Element Method, which is called CFD-iDEM (Zhang and Tahmasebi, 2022a). Here, the fluid flow is solved by the CFD based on the Distributed Lagrange Multipliers (DLM) presented by Patankar (Hager, 2014; Patankar et al., 2000), and the solid motion is computed by iDEM presented in our recent paper (Zhang and Tahmasebi, 2022a). Compared with disks in 2D or spheres in 3D simulated by the traditional DEM proposed by Cundall and Strack (Cundall and Strack, 1979), iDEM can simulate the movement of particles with complex morphology such that no simplification is imposed. Thus, we aim to take advantage of this capability and study how the morphology of particles can affect the DKT process in a coupled environment.

The rest of the paper is organized as follows. Section 2 introduces the mathematical models for fluid-particle flow. The numerical simulation setup and results are described in Section 3. Finally, Section 4 presents the conclusions.

2. Hydromechanical Modeling

The coupled fluid-particle modeling has been widely applied and the theoretical developments and major applications are well-documented elsewhere (Zhu et al., 2008, 2007). In this section, we briefly introduce the governing equations for the motion of both fluid and particles. Although the following information describes the modeling, more information is also provided in our recent papers (Zhang and Tahmasebi, 2022b, 2022a). The total computational domain for the fluid-particle flow is represented by Ω, including the particle domain Ω_p and fluid domain Ω_f. The fluid boundary not shared with the particle domain is denoted by Γ_f, and the fluid-particle interface, that is the particle boundary, is denoted by Γ_p. Considering incompressible Newtonian fluid, the governing equations for the fluid motion are given by:

$$\nabla\cdot\boldsymbol{u} = 0 \text{ in } \Omega_f \tag{1a}$$

$$\rho\left(\frac{\partial\boldsymbol{u}}{\partial t} + (\boldsymbol{u}\cdot\nabla)\boldsymbol{u}\right) = \nabla.\boldsymbol{\sigma} + \rho g\nabla z \text{ in } \Omega_f \tag{1b}$$

where $\boldsymbol{u}$ and ρ are the velocity and the density of the fluid, respectively. g is the gravitational acceleration. $\boldsymbol{\sigma}$ is the stress tensor, which has the following form:

$$\boldsymbol{\sigma} = -p\boldsymbol{I} + \boldsymbol{\tau}, \tag{2}$$

where p is the pressure. $\boldsymbol{I}$ is the identity tensor, and $\boldsymbol{\tau}$ is the viscous stress tensor. For an incompressible Newtonian fluid, $\nabla.\boldsymbol{\sigma}$ is given by:

$$\nabla\cdot\boldsymbol{\sigma} = -\nabla p + \mu\Delta\boldsymbol{u}, \tag{3}$$

where μ is the viscosity of the fluid. The boundary and initial conditions are described by:

$$\boldsymbol{u} = \boldsymbol{u}_{\partial\Omega_f}(t) \text{ on } \Gamma_f \tag{4a}$$

$$\boldsymbol{u} = \boldsymbol{u}_i \text{ on } \Gamma_p \tag{4b}$$

$$\boldsymbol{\sigma}.\boldsymbol{n} = \boldsymbol{t}_{\partial\Omega_p} \text{ on } \Gamma_p \tag{4c}$$

$$\boldsymbol{u}(t) = \boldsymbol{u}_0 \text{ in } \Omega_f \tag{4d}$$

where $\boldsymbol{u}_i$ is the velocity of the fluid-particle interface. $\boldsymbol{n}$ is the outer normal direction on the particle surface. $\boldsymbol{t}_{\partial\Omega_p}$ is the traction vector exerted on the particle surface by the fluid. With the presence of an incompressible Newtonian fluid, the fluid-particle force $\boldsymbol{F}_{f,p}$ and moment $\boldsymbol{M}_{f,p}$ need to be taken into account in particle motion, which is calculated by:

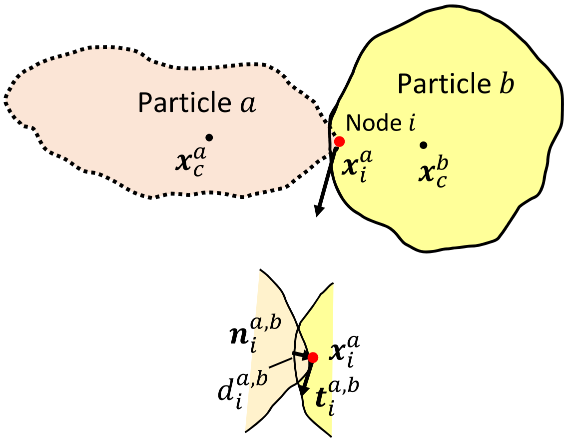

Fig. 1. Schematic of two contacting particles. The penetration has been amplified to demonstrate the overlap calculations.

Table 1
Mean drag coefficient C_D for flow over a fixed sphere at different Reynolds numbers.

Re #	20	50	100	150	300	350
Our study	2.71	1.54	1.065	0.85	0.667	0.644
Apte et al.(Apte et al., 2009)	2.62	1.55	1.1	0.9	0.686	0.649
Clift et al.(Clift et al., 1978)	2.61	1.57	1.09	0.89	0.684	0.644
Marella et al.(Marella et al., 2005)	-	1.56	1.06	0.85	0.621	-
Mittal et al.(Mittal et al., 2008)	-	-	1.08	0.88	0.68	0.63

$$\boldsymbol{F}_{f,p} = \sum_{i=1}^{N} \left(-\nabla p + \mu \Delta \boldsymbol{u}\right)_i V_i, \tag{5a}$$

$$\boldsymbol{M}_{f,p} = \boldsymbol{r} \times \boldsymbol{F}_{f,p}, \tag{5b}$$

where N is the total number of the fluid cells covered by the particle. V_i is the volume of cell i. $\boldsymbol{r}$ is the distance vector pointing from the mass center of the particle to the center of the fluid cell occupied by the particle. The detailed derivation for the fluid-particle force $\boldsymbol{F}_{f,p}$ and moment $\boldsymbol{M}_{f,p}$ can be found elsewhere (Hager, 2014; Patankar et al., 2000; Shirgaonkar et al., 2009).

When it comes to particle movement, we first consider the translational motion of the particles, which is governed by Newton's second law as follows:

$$m\ddot{\boldsymbol{x}} + C_l\dot{\boldsymbol{x}} = \boldsymbol{F}, \tag{6}$$

where m is the mass of the particle. $\ddot{\boldsymbol{x}}$ is the linear acceleration of the particle. C_l is the global damping coefficients acting on the linear velocity $\dot{\boldsymbol{x}}$. C_l is proportional to the mass, which can be expressed as $C_l = \xi m$, with ξ being the global damping constant (Cundall and Strack, 1979). $\boldsymbol{F}$ represents different forces, which are generally composed of particle-particle interaction $\boldsymbol{F}_{p,p}$, wall-particle interaction $\boldsymbol{F}_{w,p}$ and fluid-particle force $\boldsymbol{F}_{f,p}$. Particle-particle interaction $\boldsymbol{F}_{p,p}$ and wall-particle interaction $\boldsymbol{F}_{w,p}$ are caused by the collision, which can be classified as contact force. In DEM, the contact force/moment is determined by the soft-sphere model (Cundall and Strack, 1979). In the soft-sphere model, elastic and frictional forces are calculated when contacts in particle-particle or wall-particle are detected. The translational motion of particles is then described by Newton's law of motion. Before illustrating the calculation of the contact force $\boldsymbol{F}_{p,p}$ between two particles, we need to detect the contact status and overlapping/penetration value between them. For the sake of simplicity, we

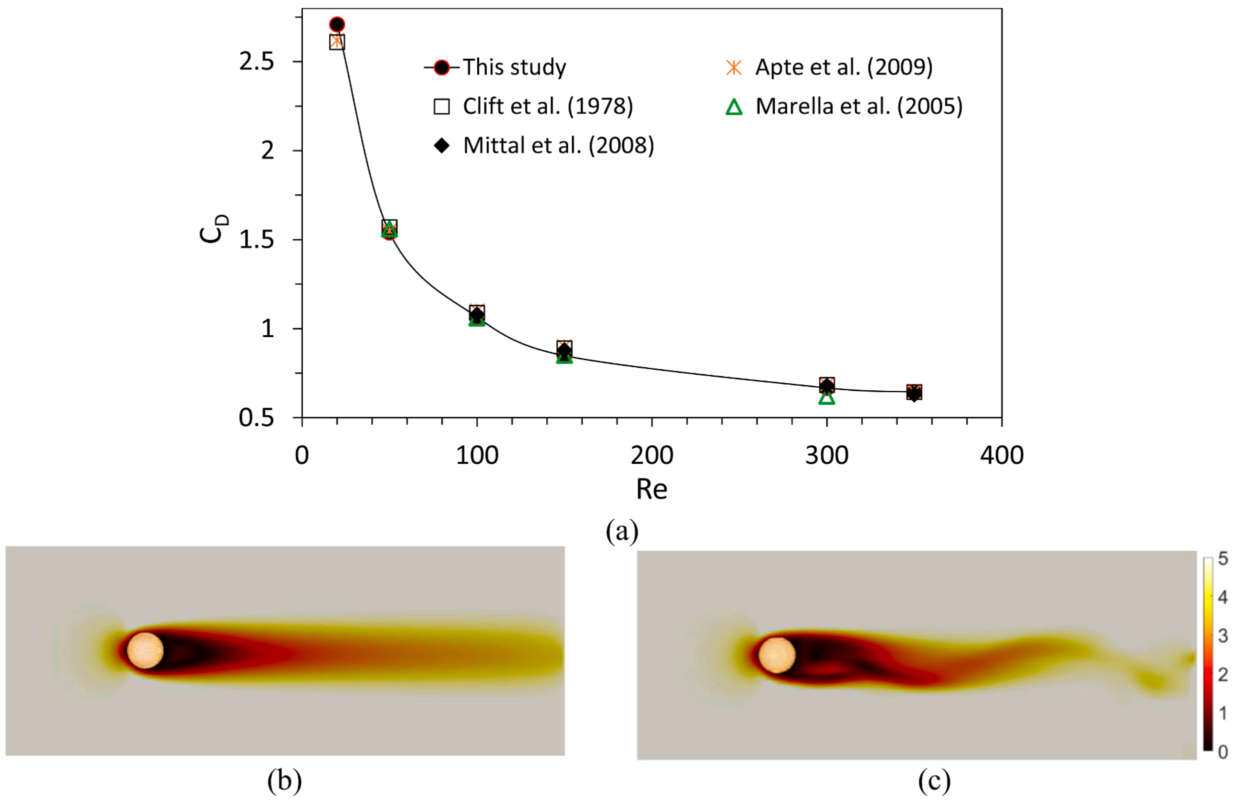

Fig. 2. (a) Comparison of mean drag coefficients with relevant studies. Flow fields around the fixed sphere at different Reynolds numbers: (b) Re = 100 and (c) Re = 500. These two maps show the velocity distribution.

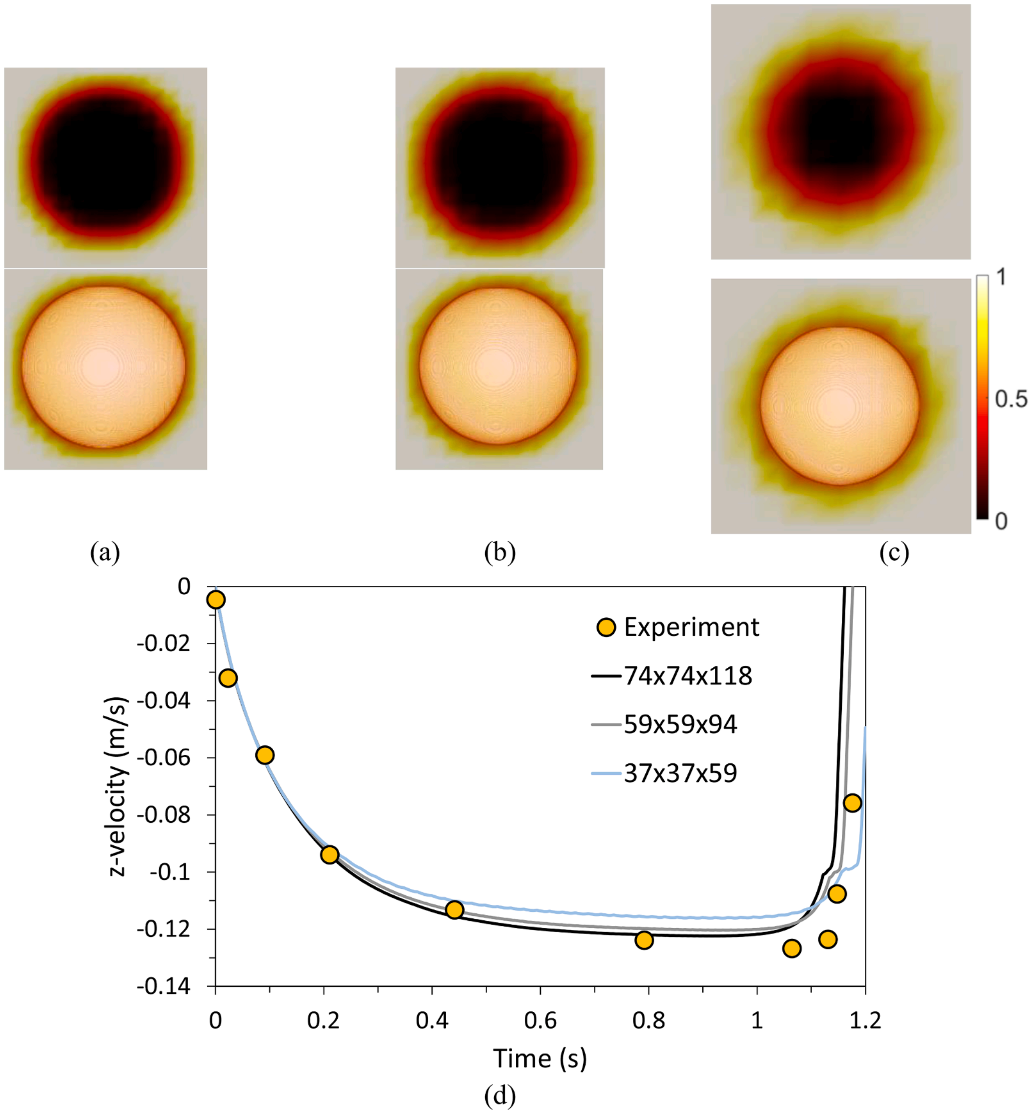

Fig. 3. Void-fraction corresponding to (a) mesh #1 ($74 \times 74 \times 118$), (b) mesh #2 ($59 \times 59 \times 94$), and (c) mesh #3 ($37 \times 37 \times 59$). (d) Comparison of the z-directional velocity of different fluid meshes with experimental data.

use two-dimensional (2D) particles to illustrate this concept, as shown in Fig. 1. Noting that the proposed method has full applicability in 3D.

Here, we take particle a as the target object to illustrate the contact detection and overlap calculation with its surrounding particle b. Thus, the following steps are taken:

1. The distance values for all nodes on the surface of particle a, referring to the distance field of particle b, are computed by the trilinear interpolation. Considering node i with position $\boldsymbol{x}_i^a$, its distance value $\Phi_b(\boldsymbol{x}_i^a)$ represents the distance from this node to the surface of particle b, and its distance gradient $\nabla\Phi_b(\boldsymbol{x}_i^a)$ represents the outward normal direction of particle b at node i.
2. If $\exists\Phi_b(\boldsymbol{x}_i^a) < 0$, that is, node i located inside of particle b, we consider the two particles to be in contact, as shown in Fig. 1. The overlap and contact normal vector at node i are calculated as:

$$d_i^{a,b} = \Phi_b\left(\boldsymbol{x}_i^a\right), \tag{7}$$

$$\boldsymbol{n}_i^{a,b} = \frac{-\nabla\Phi_b\left(\boldsymbol{x}_i^a\right)}{\|\nabla\Phi_b\left(\boldsymbol{x}_i^a\right)\|}, \tag{8}$$

where $d_i^{a,b}$ and $\boldsymbol{n}_i^{a,b}$ are the overlap and outward contact normal vector of particle a, respectively, at contact point i between particle a and particle b. The contact detection for particle a and its surrounding other particles follows the same procedure as discussed above. Similarly, when particle b is considered as the target object, the contact status with all surrounding particles is also computed in the same way.

Then, we discuss the calculation equations for the contact forces on the assumption that particle a and particle b are in contact. With the linear elastic model, the normal contact force between particle a and particle b is calculated by:

$$\boldsymbol{F}_{n,i}^a = -k_n d_i^{a,b}\boldsymbol{n}_i^{a,b}, \tag{9}$$

where $\boldsymbol{F}_{n,i}^a$ is the normal contact force exerted on particle a at contact point i. k_n is the normal elastic stiffness. By action and reaction, the normal contact force $\boldsymbol{F}_{n,i}^b$ exerted on particle b at contact point i is calculated as:

$$\boldsymbol{F}_{n,i}^b = -\boldsymbol{F}_{n,i}^a. \tag{10}$$

The resulting moments $\boldsymbol{M}_{n,i}^a$ and $\boldsymbol{M}_{n,i}^b$ at contact point i are calculated using:

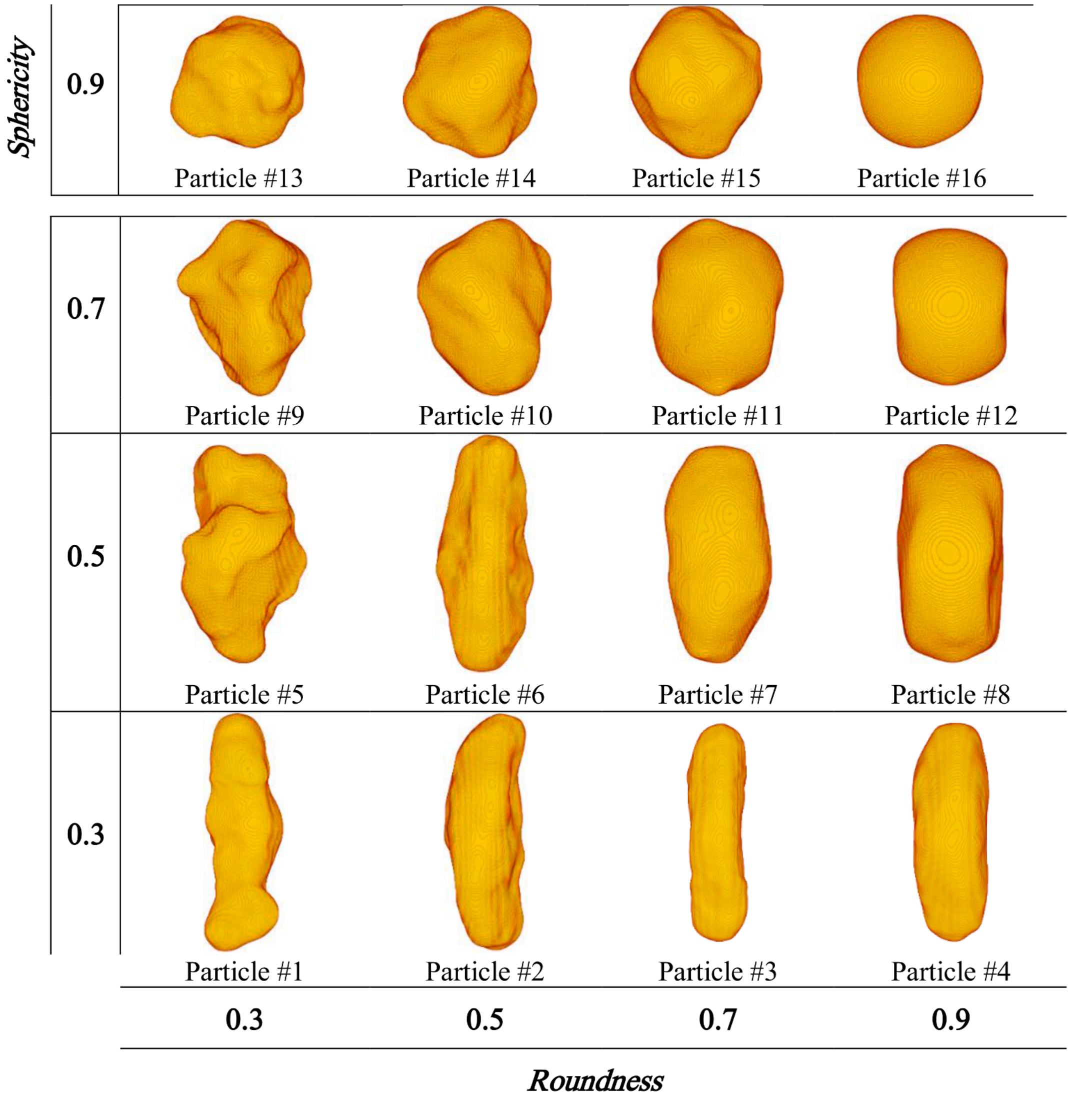

Fig. 4. Shape illustration of the considered 16 irregular particles in this study.

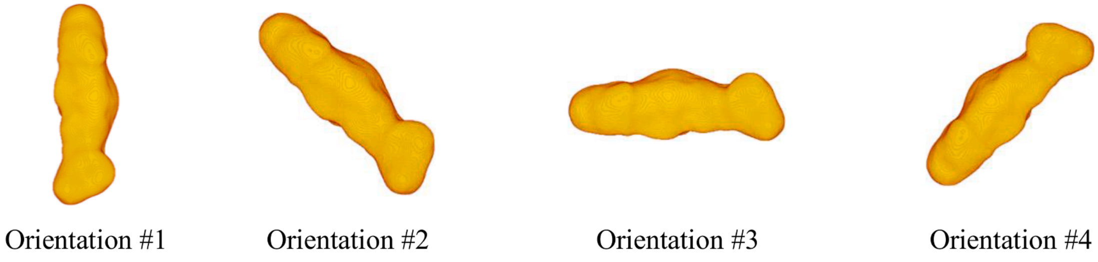

Fig. 5. Illustration of four initial orientations of particle #1

$$\boldsymbol{M}^{a}_{n,i} = \left(\boldsymbol{x}^{a}_{i} - \boldsymbol{x}^{a}_{c}\right) \times \boldsymbol{F}^{a}_{n,i}, \tag{11a}$$

$$\boldsymbol{M}^{b}_{n,i} = \left(\boldsymbol{x}^{a}_{i} - \boldsymbol{x}^{b}_{c}\right) \times \boldsymbol{F}^{b}_{n,i}, \tag{11b}$$

where $\boldsymbol{x}^a_c$ and $\boldsymbol{x}^b_c$ are the centers of mass of particle a and particle b, respectively, and $\boldsymbol{x}^a_i$ is the position of the contact point i.

The tangential contact force between particle a and particle b is calculated using the Coulomb friction model similar to the friction model. The relative velocity $\boldsymbol{v}^{a,b}$ between particle a and particle b is given by:

$$\boldsymbol{v}^{a,b} = \boldsymbol{v}^{a} + \boldsymbol{\omega}^{a} \times \left(\boldsymbol{x}^{a}_{i} - \boldsymbol{x}^{a}_{c}\right) - \boldsymbol{v}^{b} - \boldsymbol{\omega}^{b} \times \left(\boldsymbol{x}^{a}_{i} - \boldsymbol{x}^{b}_{c}\right), \tag{12}$$

where $\boldsymbol{v}^a$, $\boldsymbol{v}^b$, $\boldsymbol{\omega}^a$, and $\boldsymbol{\omega}^b$ are the linear and angular velocities of particle a and particle b, respectively. The increment in shear displacement $\Delta\zeta_i$ has the following form:

$$\Delta\zeta_{i} = \left[\boldsymbol{v}^{a,b} - \left(\boldsymbol{v}^{a,b}\cdot\boldsymbol{n}^{a,b}_{i}\right)\boldsymbol{n}^{a,b}_{i}\right]\Delta t, \tag{13}$$

where Δt is the time interval. The tangential contact force $\boldsymbol{F}^{a}_{\zeta,i}$ exerted on particle a at contact point i is calculated by:

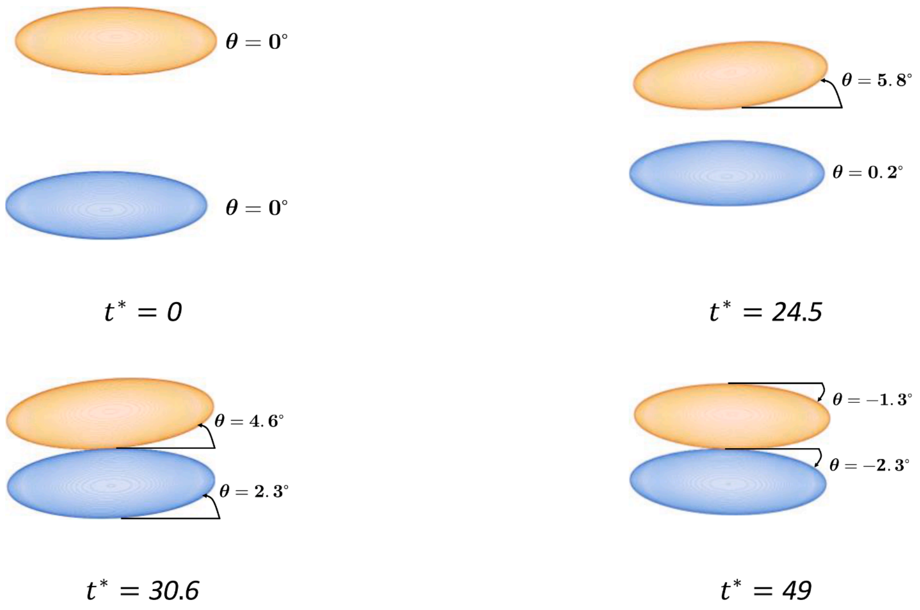

Fig. 6. Oblate particle positions in the DK process with $AR = 1/3$ at non-dimensional times $t^* = 0$, 24.5, 30.6, and 49. θ denotes the angle with respect to the y direction.

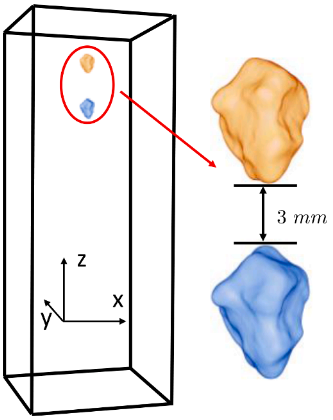

Fig. 7. Schematic of settling particle pairs of particle #9 in the state of orientation #1.

$$\left(\boldsymbol{F}^a_{\zeta,i}\right)_{t+\Delta t} = \mathscr{R}\left(\boldsymbol{F}^a_{\zeta,i}\right)_t - k_\zeta \Delta \boldsymbol{\zeta}_i, \tag{14}$$

where $\mathscr{R}$ is the rotation matrix that rotates the previous tangential contact force into the new tangential direction. Coulomb friction law limits tangential contact force $\boldsymbol{F}^a_{\zeta,i}$ to be no greater than a fraction of the normal contact force $\boldsymbol{F}^a_{n,i}$:

$$\boldsymbol{F}^a_{\zeta,i} = \frac{\boldsymbol{F}^a_{\zeta,i}}{\|\boldsymbol{F}^a_{\zeta,i}\|}\min\left(\|\boldsymbol{F}^a_{\zeta,i}\|,\ \mu\|\boldsymbol{F}^a_{n,i}\|\right), \tag{15}$$

where μ is the interparticle friction coefficient. Similarly, the tangential contact force $\boldsymbol{F}^b_{\zeta,i}$ exerted on particle b at contact point i is calculated as:

$$\boldsymbol{F}^b_{\zeta,i} = -\boldsymbol{F}^a_{\zeta,i}. \tag{16}$$

The resulting moments $\boldsymbol{M}^a_{\zeta,i}$ and $\boldsymbol{M}^b_{\zeta,i}$ at contact point i are calculated as:

$$\boldsymbol{M}^a_{\zeta,i} = \left(\boldsymbol{x}^a_i - \boldsymbol{x}^a_c\right) \times \boldsymbol{F}^a_{\zeta,i}, \tag{17a}$$

$$\boldsymbol{M}^b_{\zeta,i} = \left(\boldsymbol{x}^a_i - \boldsymbol{x}^b_c\right) \times \boldsymbol{F}^b_{\zeta,i}. \tag{17b}$$

Finally, the total contact forces and moments generated by the contact of particle a and particle b are expressed as:

$$\boldsymbol{F}^a = \sum_{i=1}^{N}\left(\boldsymbol{F}^a_{n,i} + \boldsymbol{F}^a_{\zeta,i}\right), \tag{18a}$$

$$\boldsymbol{M}^a = \sum_{i=1}^{N}\left(\boldsymbol{M}^a_{n,i} + \boldsymbol{M}^a_{\zeta,i}\right), \tag{18b}$$

$$\boldsymbol{F}^b = \sum_{i=1}^{N}\left(\boldsymbol{F}^b_{n,i} + \boldsymbol{F}^b_{\zeta,i}\right), \tag{18c}$$

$$\boldsymbol{M}^b = \sum_{i=1}^{N}\left(\boldsymbol{M}^b_{n,i} + \boldsymbol{M}^b_{\zeta,i}\right), \tag{18d}$$

where N is the total number of the contact nodes between particle a and particle b. When particle b is replaced by a wall, we can calculate the particle-wall interaction $\boldsymbol{F}_{w,p}$ generated by the contact of particle a and a wall. After the calculation of the contact forces, the particle motion controlled by Eq. (6) can be updated. To obtain the numerical solutions of the translational motion, we rewrite the motion Eq. (6) in a discrete form:

$$m\ddot{\boldsymbol{x}}^n + C_l\dot{\boldsymbol{x}}^n = \boldsymbol{F}^n, \tag{19}$$

where $C_l = \xi m$ was previously defined in Eq. (6). A central difference scheme is used to integrate Eq. (19). The evaluated linear acceleration at the current time step n has the following form:

$$\ddot{\boldsymbol{x}}^n = \frac{1}{\Delta t}\left(\dot{\boldsymbol{x}}^{n+1/2} - \dot{\boldsymbol{x}}^{n-1/2}\right). \tag{20}$$

Similarly, the evaluated linear velocity at the current time step n has the following form:

$$\dot{\boldsymbol{x}}^n = \frac{1}{2}\left(\dot{\boldsymbol{x}}^{n+1/2} + \dot{\boldsymbol{x}}^{n-1/2}\right). \tag{21}$$

The substitution of Eqs. (19)-(21) leads to the update of velocity:

$$\dot{\boldsymbol{x}}^{n+1/2} = \frac{1}{1+\xi\Delta t/2}\left[(1-\xi\Delta t\,/\,2)\dot{\boldsymbol{x}}^{n-1/2} + \frac{\Delta t}{m}\boldsymbol{F}^n\right]. \tag{22}$$

The particle position $\boldsymbol{x}$ is finally updated by the updated linear

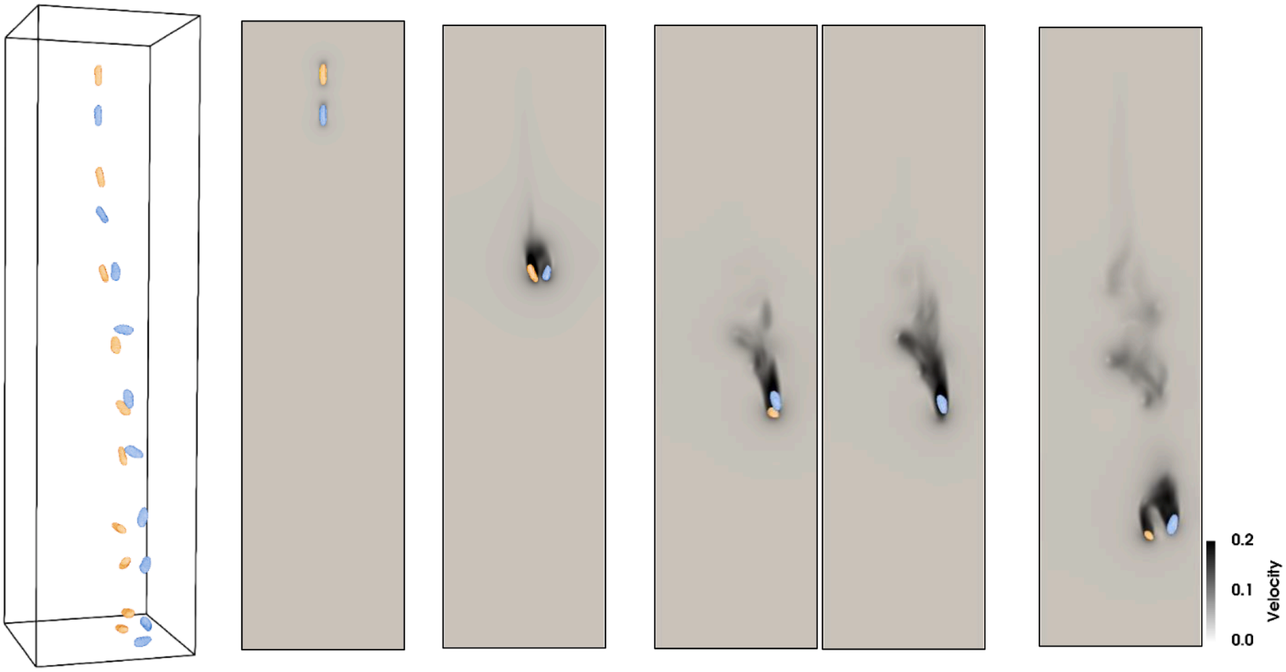

(a) (b) t=0.02 s (c) t=0.18 s (d) t=0.3 s (e) t=0.4 s

Fig. 8. (a) The trajectories of particle #4 in the state of orientation #1 in the sedimentation process (b) – (e) Velocity distribution in the DKT process at different times.

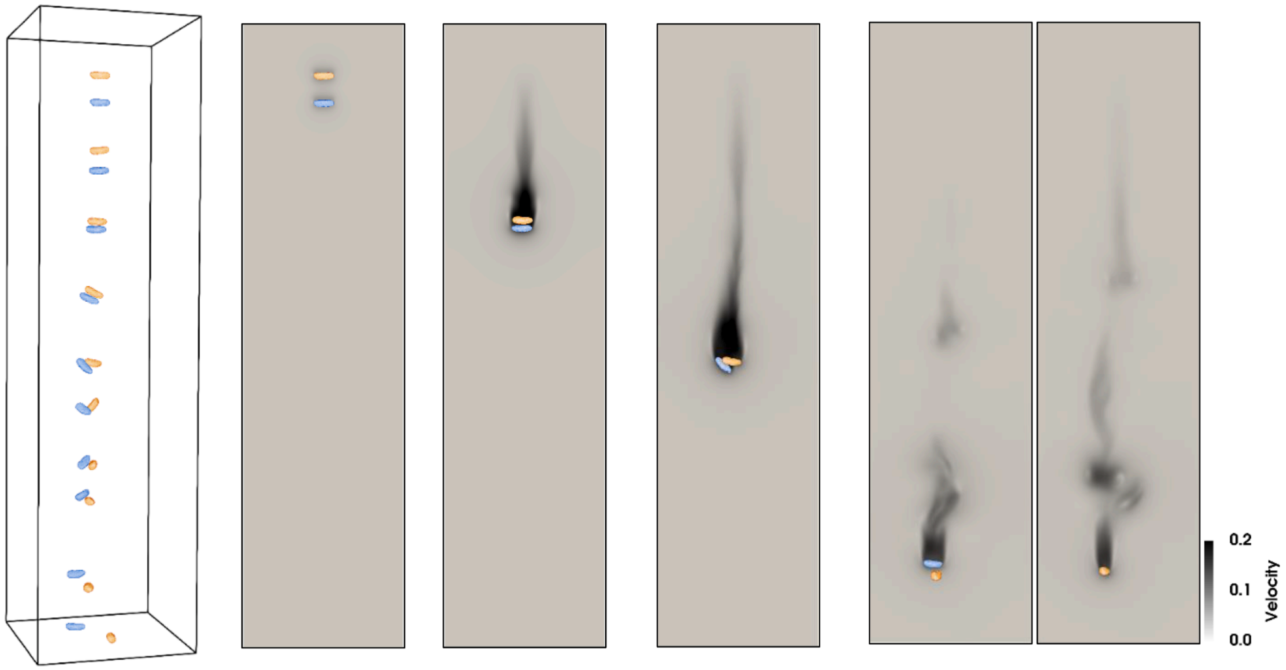

(a) (b) t=0.02 s (c) t=0.18 s (d)t=0.3 s (e) t=0.52 s

Fig. 9. (a) The trajectories of particle #4 in the state of orientation #3 in the sedimentation process (b) – (e) Velocity distribution in the DKT process at different times.

velocity, respectively.

$$\boldsymbol{x}^{n+1} = \boldsymbol{x}^{n} + \Delta t \dot{\boldsymbol{x}}^{n+1/2}. \tag{23}$$

When it comes to the rotational motion of the particle, it is advantageous to deal with it in the principal body-fixed frame of the particle. For the rest of this section about the rotational motion, the rotational quantities are defined in the principal body-fixed frame unless explained otherwise. The angular accelerations $\ddot{\theta}_i, i = 1, 2, 3$ are calculated by the Euler's equations of motion, which are shown in 3D as follows:

$$\ddot{\theta}_1 = [M_1 + \omega_2\omega_3(I_2 - I_3) - \xi I_1\omega_1] \Big/ I_1, \tag{24a}$$

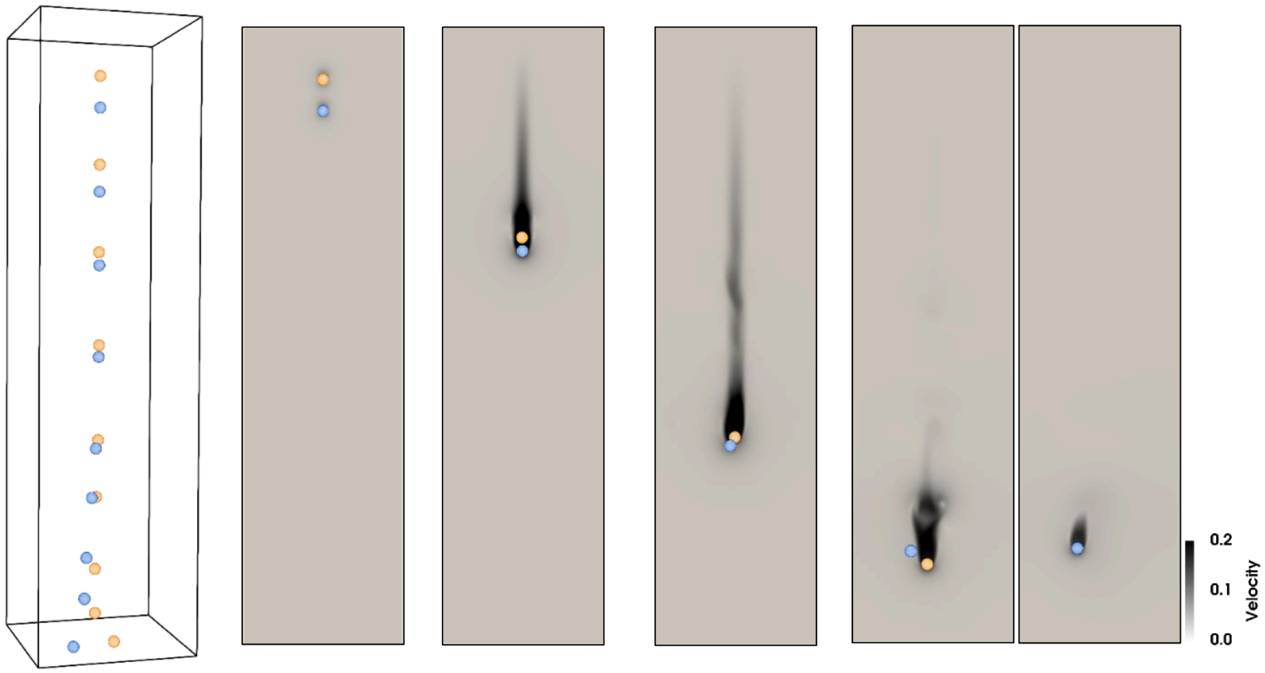

(a) (b) t=0.02 s (c) t=0.18 s (d) t=0.3 s (e) t=0.4 s

Fig. 10. (a) The trajectories of particle #17 (sphere) in the sedimentation process (b) – (e) Velocity distribution in the DKT process at different times.

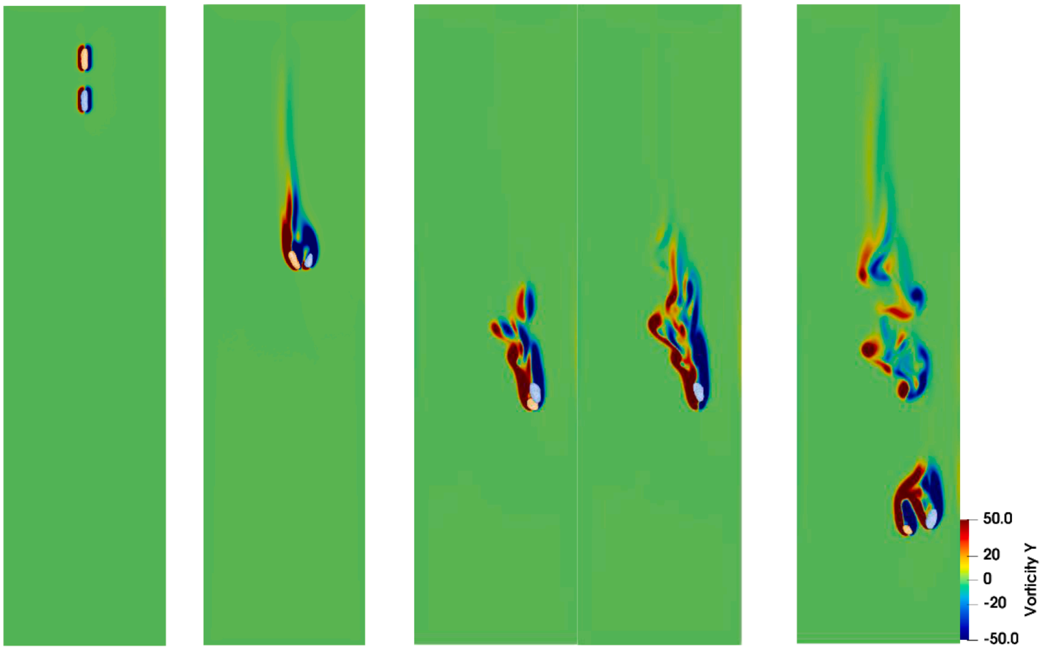

(a) t=0.02 s (b) t=0.18 s (c) t=0.3 s (d) t=0.4 s

Fig. 11. Vorticity contour in the DKT process of particle #4 in the state of orientation #1 at different times.

$$\ddot{\theta}_2 = [M_2 + \omega_3\omega_1(I_3 - I_1) - \xi I_2\omega_2]/I_2, \tag{24b}$$

$$\ddot{\theta}_3 = [M_3 + \omega_1\omega_2(I_1 - I_2) - \xi I_3\omega_3]/I_3, \tag{24c}$$

where ω_i for $i = 1, 2, 3$ are the three components of the angular velocities. M_i for $i = 1, 2, 3$ are the three components of the moments exerted on the particle. I_i for $i = 1, 2, 3$ are the three components of the moment of inertia. The above Euler equations are nonlinear due to the presence of the products of ω on the right-hand side. To integrate the rotational motion, a predictor-corrector algorithm is utilized (Lim and Andrade, 2014; Walton and Braun, 1993). This approach undertakes the subsequent steps:

1. Angular velocities at the present time step can be projected by considering a constant ω for an extra half step:

$$\omega'^{n}_i = \omega_i^{n-1/2} + \frac{1}{2}\Delta\omega_i^{n-1}, \ i = 1, 2, 3 \tag{25}$$

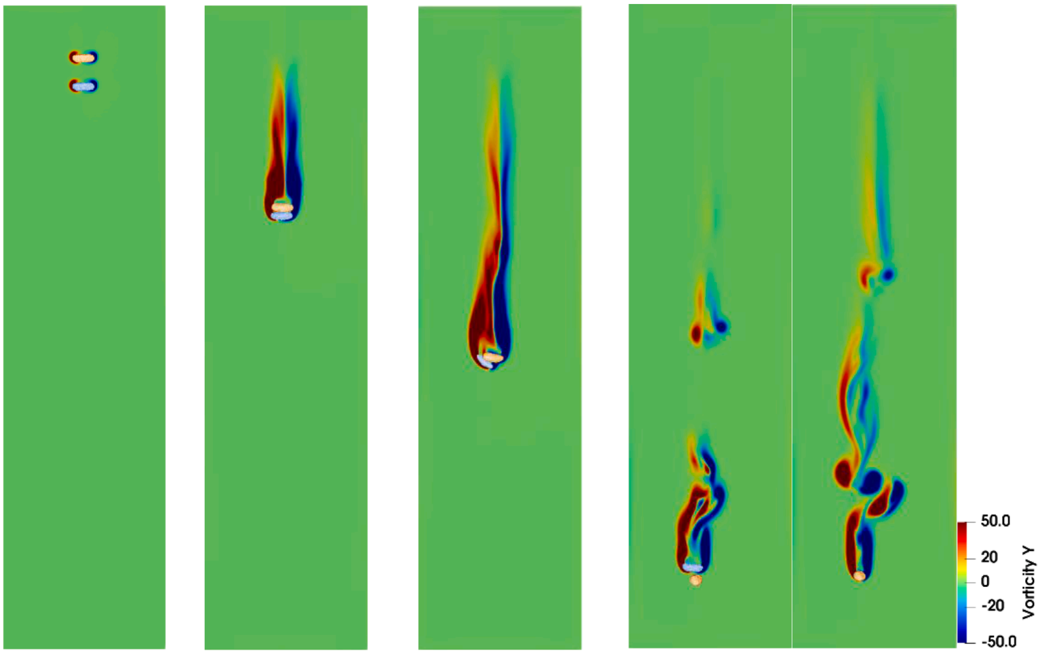

(a) t=0.02 s (b) t=0.18 s (c)t=0.3 s (d) t=0.52 s

Fig. 12. Vorticity contour in the DKT process of particle #4 in the state of orientation #3 at different times.

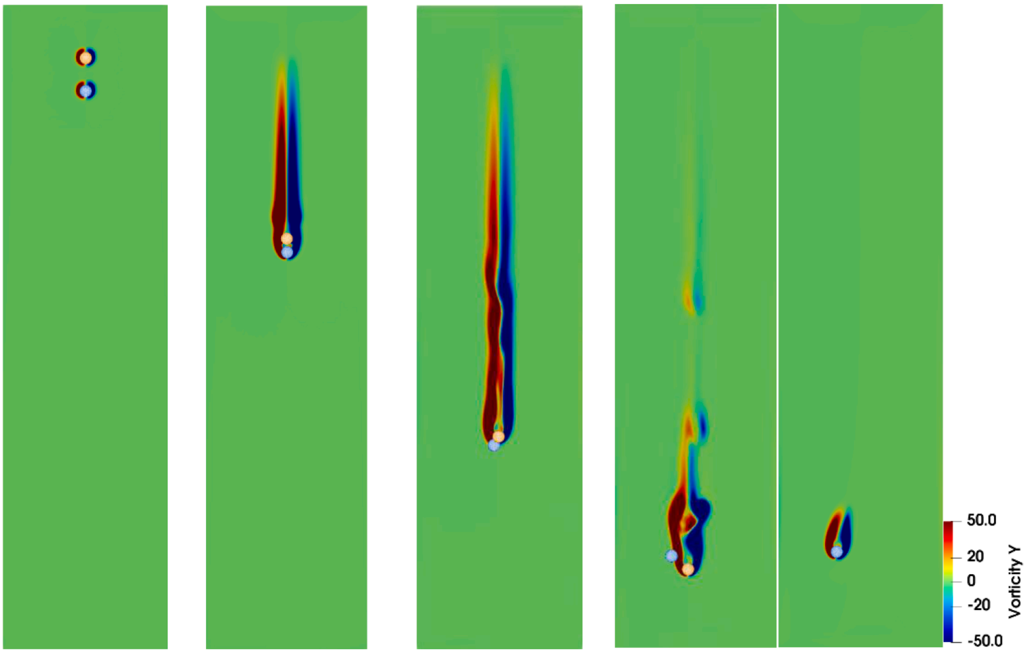

(a) t=0.02 s (b) t=0.18 s (c) t=0.3 s (d) t=0.4 s

Fig. 13. Vorticity contour in the DKT process of particle #17 (sphere) at different times.

2. A first prediction of ω at the present time step can be obtained by these extrapolated ω along with the current moments:

$$\Delta\omega'^{n}_{1} = \Delta t\left[M^{n}_{1} + \omega'^{n}_{2}\omega'^{n}_{3}(I_2 - I_3) - \xi I_1\omega'^{n}_{1}\right]/I_1, \tag{26a}$$

$$\Delta\omega'^{n}_{2} = \Delta t\left[M^{n}_{2} + \omega'^{n}_{3}\omega'^{n}_{1}(I_3 - I_1) - \xi I_2\omega'^{n}_{2}\right]/I_2, \tag{26b}$$

$$\Delta\omega'^{n}_{3} = \Delta t\left[M^{n}_{3} + \omega'^{n}_{1}\omega'^{n}_{2}(I_1 - I_2) - \xi I_3\omega'^{n}_{3}\right]/I_3. \tag{26c}$$

3. Then, these predicted ω are utilized to predict ω more accurately at the present time step:

$$\omega^{n}_{i} = \omega^{n-1/2}_{i} + \frac{1}{2}\Delta\omega'^{n}_{i}. \tag{27}$$

4. The corrected ω are then described by:

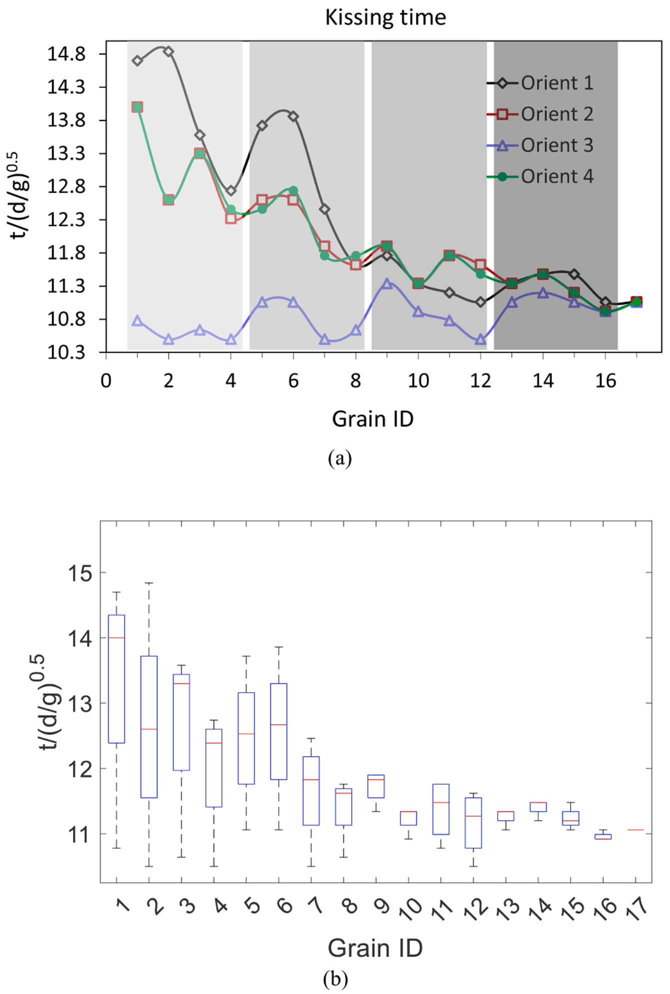

(a)

(b)

Fig. 14. Kissing time for the 65 models. (a) Each sphericity is grouped in a different block shown using separate gray color intensities. (b) The boxplot distribution of each grain ID where the minimum, lower quantile, median, and upper quantile values are shown through which the variability among the considered orientations can be observed.

$$\Delta\omega_1^n = \Delta t\left[M_1^n + \omega_2^n\omega_3^n(I_2 - I_3) - \xi I_1\omega_1^n\right]/I_1, \tag{28a}$$

$$\Delta\omega_2^n = \Delta t\left[M_2^n + \omega_3^n\omega_1^n(I_3 - I_1) - \xi I_2\omega_2^n\right]/I_2, \tag{28b}$$

$$\Delta\omega_3^n = \Delta t\left[M_3^n + \omega_1^n\omega_2^n(I_1 - I_2) - \xi I_3\omega_3^n\right]/I_3. \tag{28c}$$

Further iterations of Eqs. (27) – (28) are performed until a convergence criterion based on the changes in quantities $\Delta\omega_i^n, i = 1, 2, 3$ between successive iterations is satisfied, or a predetermined number of iterations is reached.

5. Finally, these corrected ω can be used to update the angular velocities to the midpoint of the next timestep:

$$\omega_i^{n+1/2} = \omega_i^{n-1/2} + \Delta\omega_i^n. \tag{29}$$

Euler's equations have singularities when the angle is zero. Thus, after obtaining ω, the orientation of the principal body-fixed frame is revised using an adaptation of Evans' singularity free quaternion algorithm (Evans and Murad, 2006) through which four quaternions are mutually dependent and orthogonal are used to substitute Euler angles and subsequently build the motion equations. For Euler's equations of motion, the quantities are defined in the principal body-fixed frame for each non-spherical body while the contact detection and force calculations are calculated in a space/global reference frame. The rotation matrix which transforms the space frame to the body frame is described by:

$$\mathbf{A} = \begin{pmatrix} -q_1^2 + q_2^2 - q_3^2 + q_4^2 & -2(q_1q_2 - q_3q_4) & 2(q_2q_3 + q_1q_4) \\ -2(q_1q_2 + q_3q_4) & q_1^2 - q_2^2 - q_3^2 + q_4^2 & -2(q_1q_3 - q_2q_4) \\ 2(q_2q_3 - q_1q_4) & -2(q_1q_3 + q_2q_4) & -q_1^2 - q_2^2 + q_3^2 + q_4^2 \end{pmatrix}, \tag{30}$$

where q_i (i.e., quaternions) are defined by:

$$q_1 = \sin\left(\frac{\theta}{2}\right)\sin\left(\frac{\psi - \phi}{2}\right), \tag{31a}$$

$$q_2 = \sin\left(\frac{\theta}{2}\right)\cos\left(\frac{\psi - \phi}{2}\right), \tag{31b}$$

$$q_3 = \cos\left(\frac{\theta}{2}\right)\sin\left(\frac{\psi + \phi}{2}\right), \tag{31c}$$

$$q_4 = \cos\left(\frac{\theta}{2}\right)\cos\left(\frac{\psi + \phi}{2}\right), \tag{31d}$$

and ϕ, θ, and ψ are the Euler's angles in the $zx'z'$ notational convention (Goldstein, Herbert; Poole, C. P.; Safko, 2001). The initial configurations of the particles provide the values for the initial quaternions at the initial state of the simulation.

The time derivatives of the quaternions can be calculated by the products of the quaternions and the angular velocities as a singularity-free set of equations (Evans and Murad, 2006):

$$\begin{pmatrix} \dot{q}_1 \\ \dot{q}_2 \\ \dot{q}_3 \\ \dot{q}_4 \end{pmatrix} = \frac{1}{2}\begin{pmatrix} -q_3 & -q_4 & q_2 \\ q_4 & -q_3 & -q_1 \\ q_1 & q_2 & q_4 \\ -q_2 & q_1 & -q_3 \end{pmatrix}\begin{pmatrix} \omega_1 \\ \omega_2 \\ \omega_3 \end{pmatrix}. \tag{32}$$

It should be noticed that only three of the quaternions are independent and the closure of this system is achieved by the normalization constraint:

$$\sum_{i=1}^{4} q_i^2 = 1. \tag{33}$$

The quaternions at the new time step can be obtained by explicitly solving Eq. (32) by the time-centered finite difference scheme (Walton and Braun, 1993), which gives rise to the following equation:

$$\boldsymbol{q}^{n+1} = \boldsymbol{B}^{-1}\boldsymbol{B}^T\boldsymbol{q}^n, \tag{34}$$

where

$$\boldsymbol{q}^n = \begin{pmatrix} q_1^n \\ q_2^n \\ q_3^n \\ q_4^n \end{pmatrix}, \boldsymbol{B} = \begin{pmatrix} 1 & -\beta_3 & \beta_1 & \beta_2 \\ \beta_3 & 1 & \beta_2 & -\beta_1 \\ -\beta_1 & -\beta_2 & 1 & -\beta_3 \\ -\beta_2 & \beta_1 & \beta_3 & 1 \end{pmatrix}, \tag{35}$$

and

$$\beta_i = \frac{\Delta t}{4}\omega_i^{n+1/2}. \tag{36}$$

The matrix $\mathbf{A}^{n+1}$ of Eq. (30) at t_{n+1} can be updated using the new quaternions $\boldsymbol{q}^{n+1}$. The orientation of the principal body-fixed frame is then updated by the rows of $\mathbf{A}^{n+1}$. In the next calculation cycle, the moments on each particle due to interparticle contact, calculated in the

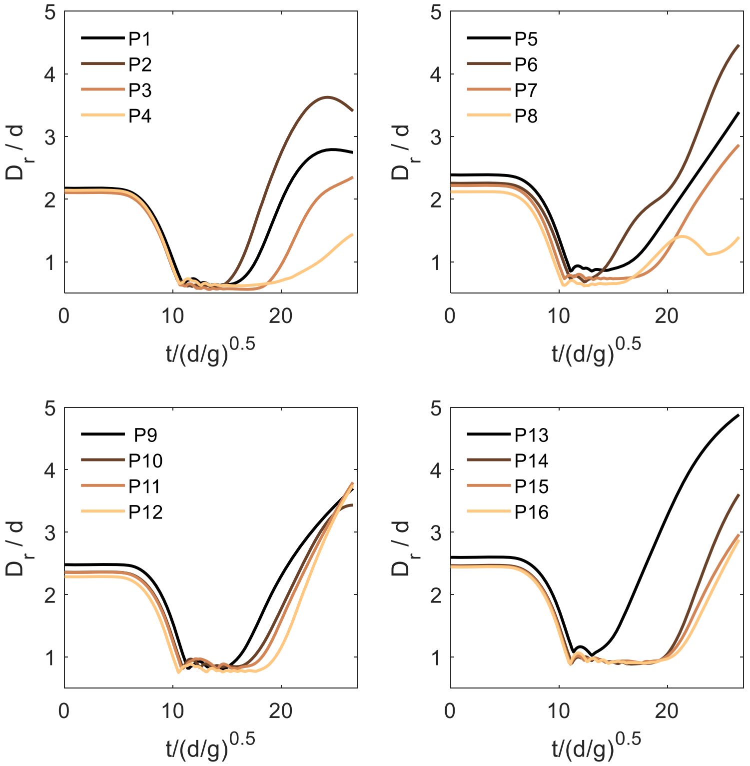

Fig. 15. The comparison of gap D_r of different particle pairs with orientation #3 in the same row shown in Fig. 4.

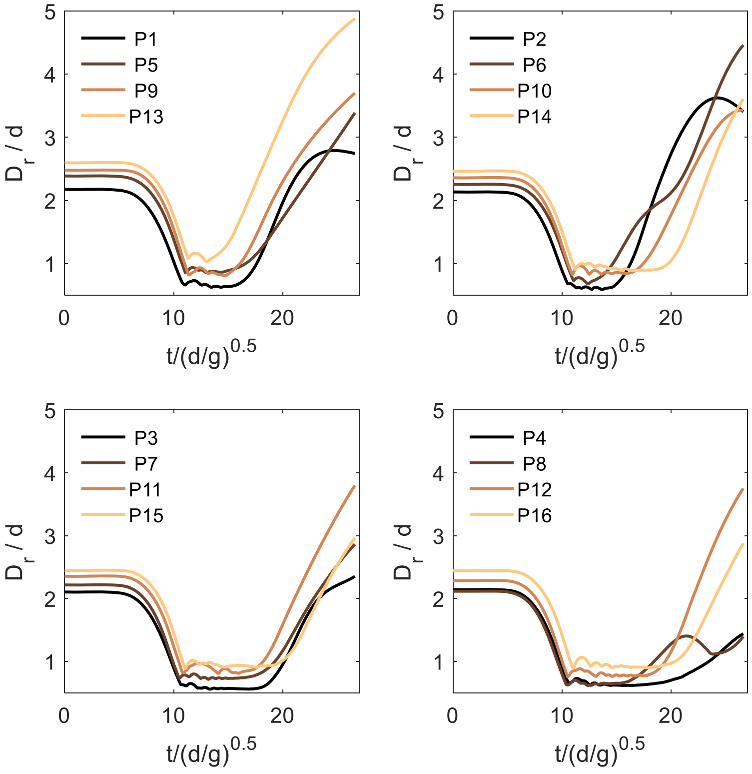

Fig. 16. The comparison of gap D_r of different particle pairs with orientation #3 in the same column shown in Fig. 4.

global frame, are transformed into the principal body-fixed frame using $\mathbf{A}^{n+1}$:

$$\boldsymbol{M}_B^{n+1} = \left(\mathbf{A}^{n+1}\right)^T \boldsymbol{M}_G^{n+1}, \tag{37}$$

where $\boldsymbol{M}_B^{n+1}$ and $\boldsymbol{M}_G^{n+1}$ are the moments in the principal body-fixed frame and global frame, respectively.

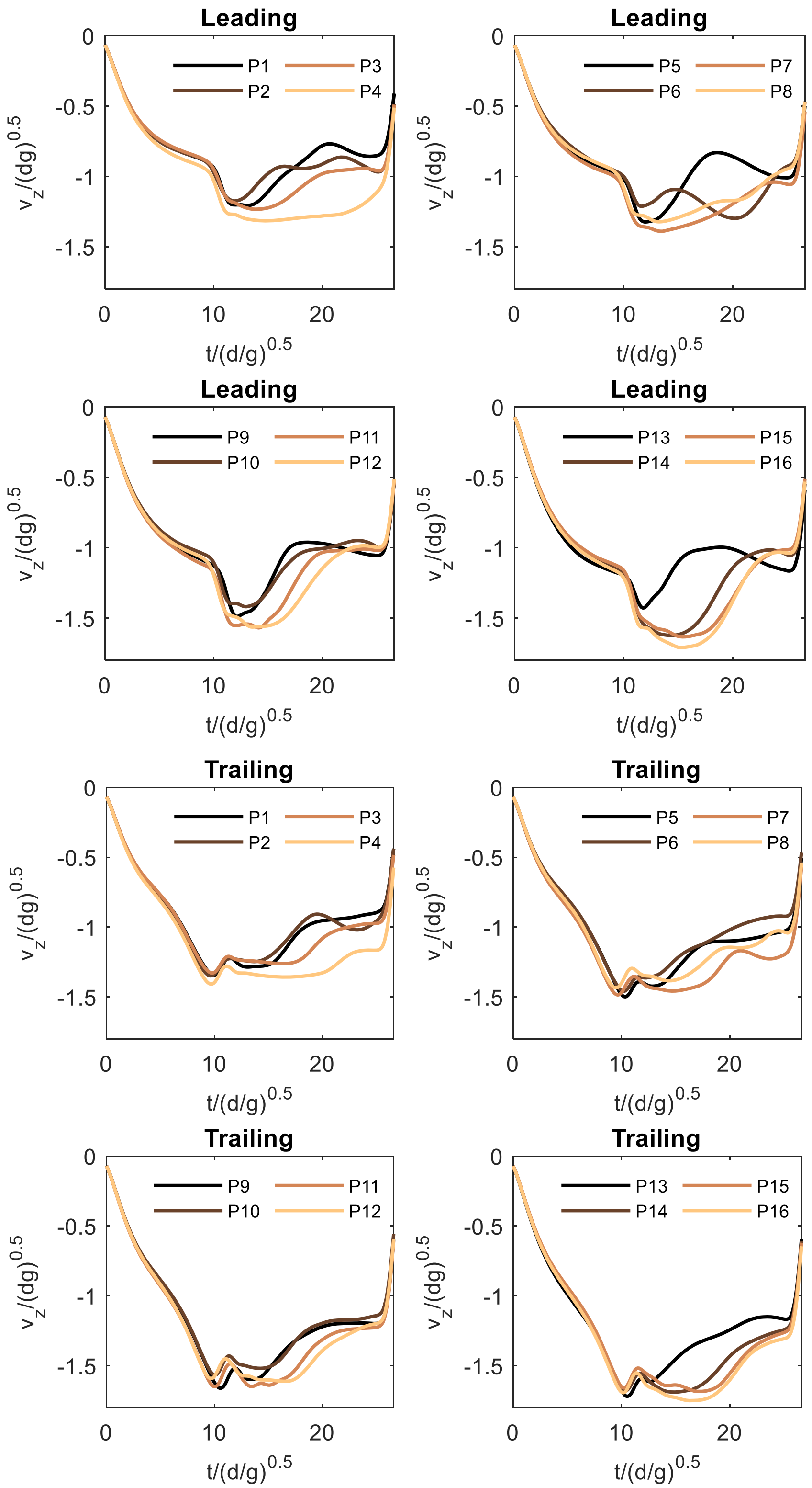

Fig. 17. The comparison of vertical velocity $v_z/\sqrt{dg}$ of different particle pairs with orientation #3 in the same row shown in Fig. 4.

3. Numerical Simulation

3.1. Validation of coupled CFD-iDEM

Before demonstrating the results, we resort to two different cases to verify the accuracy of the coupled CFD-iDEM: flow over a fixed sphere and the settlement of one sphere. First, the mean drag coefficient C_D for flow over a fixed sphere at different Reynolds numbers (Re) are calculated by our simulations and the results are compared with other studies. The simulation domain size is $15d_p \times 6d_p \times 6d_p$ (d_p is the sphere diameter) in x, y, and z directions, respectively, with the boundary conditions: inflow and convective outflow conditions in the x directions and slip-conditions in the y and z directions. Here, the fluid inflow velocity is set as $u_\infty = 5\ m/s$ and fluid density is $\rho_f = 1000\ kg/m^3$ while the fluid

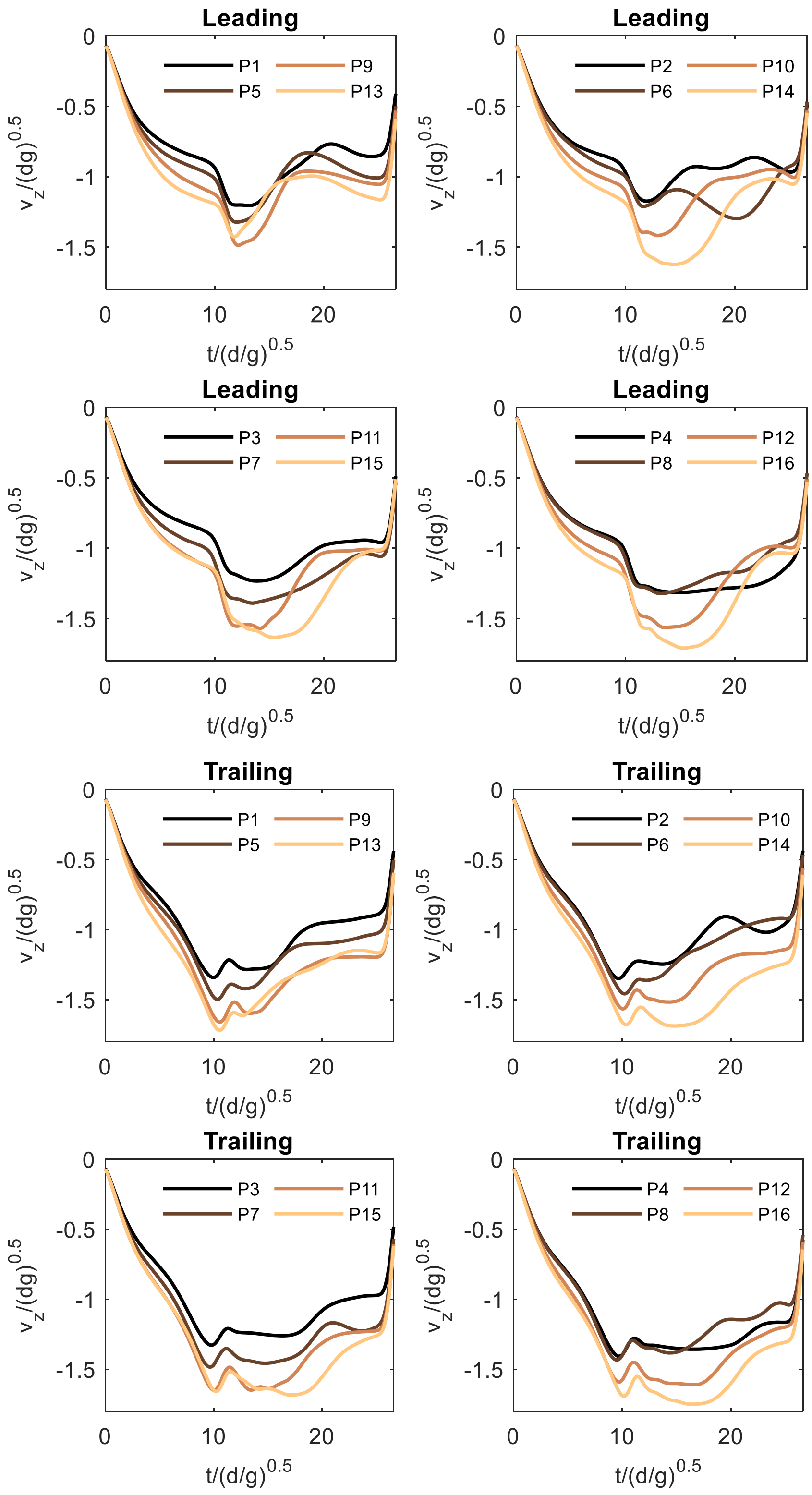

Fig. 18. The comparison of vertical velocity $v_z/\sqrt{dg}$ of different particle pairs with orientation #3 in the same column shown in Fig. 4.

viscosity μ_f is considered to vary with different Reynolds numbers. Table 1 and Fig. 2(a) show the comparison of the mean drag coefficients with other studies, and a good agreement can be noticed. Furthermore, the flow fields around the fixed sphere with Re $= 100$ and Re $= 500$ can be observed in Figs. 2(b) and 2(c), respectively.

Along with the comparison of drag coefficients, the effect of the fluid computational cells on the simulation accuracy can be investigated by the settlement of one particle, which has been done frequently in previous studies. The simulation conditions are corresponding to the experimental study reported in(Ten Cate et al., 2002) and the simulation study by Apte et al. (Apte et al., 2009). The spherical particle density in the settlement is $\rho_p = 1120\ kg/m^3$ and the diameter is $d_p = 15\ mm$. The settlement takes place in a domain with the size of $100\times\ 100\times\ 160\ mm^3$. The particle is centrally located in the x and y directions and is 120 *mm* away from the bottom in the *z* direction at the initial time. The fluid density is $\rho_f = 960\ kg/m^3$ and fluid viscosity is $\mu_f = 58 \times 10^{-3} Pa{\cdot}s$. No-slip boundaries are set for the walls. We investigate the simulation results corresponding to three different fluid cell resolutions, namely $74 \times 74 \times 118$ (mesh #1), $59 \times 59 \times 94$ (mesh #2), and $37 \times 37 \times 59$ (mesh #3). The effect of fluid cell resolutions on the calculated void-fraction can be observed in Fig. 3(a-c), which shows that the void-fraction becomes blurrier and less accurate when the fluid cell resolution decreases from mesh #1 to mesh #3. The comparison of particle *z*-velocity in Fig. 3(d) reveals that the simulation results of mesh #1 and mesh #2 are in good agreement with the experimental data while the error increases with the fluid mesh being coarser (Ten Cate et al., 2002).

3.2. Settlement of two particles

To investigate the effect of particle shape on the DKT process, we have chosen 16 irregular particles (Fig. 4) and one spherical particle to symmetrically study the DKT phenomenon. These particles originate from the X-ray computed tomographic (XRCT) images of real particles and are represented by distance values obtained by the improved distance transformation (Zhang and Tahmasebi, 2022a). The 16 irregular particles have different sphericity (*S*) and roundness (*R*) as shown in Fig. 4 (Krumbein, 1941; Powers, 1953; Wadell, 1932). Krumbein defined the sphericity as:

$$S = \sqrt[3]{bc/a^2}, \tag{38}$$

where *a* for the long axis, *b* for the intermediate axis, and *c* for the short axis of the three representative axes of one particle. Wadell defined roundness as the ratio of the average radius of curvature of the corners of one particle to the radius of its maximum inscribed sphere:

$$R = \frac{\frac{1}{n}\sum_{i=1}^{n} r_i}{r_{max-in}}, \tag{39}$$

where r_i is the radius of the *i*-th corner curvature, *n* the number of corners, and r_{max-in} the radius of the maximum inscribed sphere. The 17 particles (16 irregulars plus one spherical) have the same density $\rho_p = 1.5 \times 10^3$ and same mass m_p, which means the same equivalent sphere diameter calculated by $d = 2 \times \left(\frac{3m_p}{4\pi\rho_p}\right)^{1/3}$. Here, the equivalent sphere diameter for all the particles is $d = 2\ mm$. Moreover, each particle has four initial orientations, generated by rotating the particles along *y* axis with the angle interval of 45°, meaning that four angles of 0°, 45°, 90° and 135° are used. The four initial orientations are illustrated by particle #1 in Fig. 5. Therefore, there are 65 models in this study: 4 models for each irregular particle and one model for the spherical particle.

3.2.1. Settlement of oblate particle pairs

M.N.Ardekani et al. have numerically studied the sedimentation of spheroidal particles (Ardekani et al., 2016). It is therefore meaningful to study our DKT results of spheroidal particles based on their cases before simulating the sedimentation process for the irregular particles as illustrated previously. We have chosen the case of oblate particle pairs and set model parameters based on their studies (Ardekani et al., 2016). For example, the aspect ratio *AR* being 1/3; the density ratio between particle and fluid being 1.14; the Galileo number Ga being 80. The initial position of the center of the lower particle is set to be $0.5L_x$, $0.5L_y$, and $0.8L_z$, where $L_x = 5d_{eq}$, $L_y = 5d_{eq}$ and $L_x = 15d_{eq}$ are the dimensions of the simulation domain. Periodic boundary conditions are imposed in both *x* and *y* directions whereas a free surface and no-slip wall are used at the upper and bottom boundary. The upper particle is above the lower particle and the vertical distance between the particle surface is set as d_{eq}. Moreover, the y-coordination of the lower oblate particle is $0.1d_{eq}$ less than the upper oblate particle.

Fig. 6 shows the drafting and kissing process of the oblate particle pairs with an aspect ratio $AR = 1/3$. It can be observed that the trailing particle, initially located above and on the right-hand side of the leading particle, experiences positive y-inclination due to the torque difference between the right and left side exerted on the trailing particle from the ambient fluid. With this orientation, the distance gap between the particle pairs in the horizontal direction gradually decreases when the trailing particle is approaching the leading particle. Eventually, the two particles are in contact and their orientation gradually keeps stable with their major axis perpendicular to the fluid streamline direction. This movement validates the points from the studies of M.N.Ardekani et al. (Ardekani et al., 2016), that is the settling spheroids can resist horizontal motion by adjusting the particle's orientation so that their broad side keeps perpendicular to the fluid streamline direction.

3.2.2. Model Setup

In the sedimentation simulations, the particle pairs composed of two identical particles are located in the domain of $25 \times 25 \times 97.5\ mm^3$. The fluid density is $\rho_f = 1000\ kg/m^3$ and fluid viscosity is $\mu_f = 1 \times 10^{-3} Pa{\cdot}s$. No-slip boundaries are set for the walls and each fluid computational cell size is $0.25 \times 0.25 \times 0.25\ mm^3$ (corresponding to mesh #2 in Fig. 3(b)). Initially, the two particles are located at the channel centerline with a specified vertical distance which is proportional to the average size of particles. Here, the initial vertical distance refers to the *z*-directional distance between the bottom surface of the upper/trailing particle and the top surface of the lower/leading particle at the initial time, as shown in Fig. 7. The initial vertical distance between the particle pairs is set as $1.5d_p = 3\ mm$ for all the 65 models.

3.2.3. DKT results

The sedimentation of two particles, as mentioned earlier, undergoes a phenomenon known as Drafting–Kissing–Tumbling (DKT), which has been reproduced in our simulation. The DKT process can be observed for three cases from the successive movements in Figs. 8(a), 9(a), and 10(a). We present the DKT process of particle #4 in the state of orientation #1 and orientation #3, and particle #17 (sphere) in those figures, respectively. In the sedimentation process, the lower pressure in the wake of the leading particle results in the larger velocity of the trailing particle which helps it to gradually catch up with the leading particle. This step is called drafting. The continuing reduction of the distance between the two particles eventually leads them to touch each other, which is called kissing. The unstable vertical alignment makes the trailing particle push the leading one aside and take the lead (tumbling stage). It can be noticed that there are two velocity slices in Figs. 8(d), 9(e), and 10(e). These two velocity slices are obtained at the same time but in different *y*-directional positions because the particle pairs are not in the same *y* plane as they can freely move in that direction. We, therefore, put two *y*-slices to demonstrate the velocity distribution around each particle. It can be noticed that the DKT process is more complicated for particle #4 of orientation #1, in which the trailing particle changed its role twice: trailing state - leading state, leading state - trailing state (a similar situation for the leading particle).

The fluid velocity distributions in Figs. 9 and 10 show that there are rare horizontal and rotational movements in the motion of particle pairs because the fluid flow velocities take place mainly at the regional center and concentrate in the vertical direction. The phenomena are reasonable because the broad side of the particle pairs in Figs. 9 and 10 is perpendicular to the fluid streamline direction at the initial time, and therefore there is no need to take horizontal and rotational movements to adjust the orientation of particle pairs. On the contrary, both the fluid velocity distribution and the movement of particle pairs in Fig. 8 show that particle #4 in the state of orientation #1 undergoes a complicated drafting stage because the particle pairs tend to adjust their orientation by the hydrodynamic force exerted on the particles to reach the stable status which is represented by the broad side of the particle pairs perpendicular to the fluid streamline direction. The deviated and dispersed fluid velocity distribution in Fig. 8 is the result of both the horizontal and rotational movements of the particle pairs. In the kissing and tumbling stages, the particle pairs are in contact and the trailing particle gradually pushes the leading particle aside until the separation happens. The tumbling movement shown in Figs. 8-10 is the result of the unstable alignment of the particle pairs in the vertical direction which represents the particle pairs cannot stay one behind the other with the ambient viscous fluid. The off-centered and dispersed fluid velocity distribution in the kissing-tumbling process shown in Figs. 8-10 reflects the horizontal and rotational movements of particle pairs. Moreover, compared to the DKT process shown in Figs. 9-10, the DKT process happened twice shown in Fig. 8, which is reflected by the phenomenon that the trailing (or leading) particle changed its role twice: trailing state - leading state, leading state - trailing state. The complicated particle settlement process in Fig. 8 reflects that the separation of the particle pairs after the first tumbling stage is not complete. The fluid fields around the particle pairs can still capture and affect the motion of the other particle, which induces the second DKT process. This phenomenon can be better illustrated by the vortex structures of the particle pairs in the next.

To better represent the behaviors of particles in the DKT process, we also have studied the vorticity of such systems in different time steps and have compared the results. Figs. 11-13 exhibit the distribution of y-vorticity around the particle pairs corresponding to their position states shown in Figs. 8-10, respectively. In the cases of particle #4 in the state of orientation #3 and particle #17 (shown in Figs. 12 and 13, respectively), a pair of the vortex is formed behind the particles and is lengthened as particle settling, and the distribution of the y-vorticity is similar in these two cases in the drafting stage. However, in the case of particle #4 in the state of orientation #1 (shown in Fig. 11), the evolution of the vorticity is more complicated and even begins to shed in the drafting stage, different from the cases of particle #4 in the state of orientation #3 and particle #17. The asymmetry of the vorticity structure in Fig. 11 induces the rotation of particles in the drafting stage. The large rotation of particles in the case of particle #4 in the state of orientation #1 is reasonable because the irregular particles can adjust their orientations to keep their broad-side perpendicular to the fluid streamline direction (Ardekani et al., 2016). When the particle pairs enter the kissing and tumbling stages, the shed vortex for all the settlements shown in Figs. 11-13 is clear, which is conducive to particle rotation and separation. The vortex structures of the particle pairs have no interaction with each other after the two particles completely separate, which can be observed in Figs. 11(d), 12(d), and 13(d). Fig. 8(a) shows one complicated particle settlement process during which the trailing particle changes its role twice: trailing state - leading state, leading state - trailing state (a similar situation for the leading particle). These behaviors can be explained by the vortex structures of the particle pairs (shown in Figs. 11(b)-(c)), which keep interacting with each other and hinder the particle's complete separation. For example, when the trailing particle was first in contact with the leading particle, took the lead and separated with the leading particle, the vortex structures of the particle pairs failed to completely separate and therefore resulted in the second KT (kissing and tumbling stages) process until there was no interaction between the vortex structures (shown in Fig. 11(b)). We will further investigate the DKT process quantitively next.

Time development of the gap D_r between the particle pairs can give a better view of the DKT process: $D_r = \sqrt{(x_1 - x_2)^2 + (y_1 - y_2)^2 + (z_1 - z_2)^2}$, where the (x_1, y_1, z_1) and (x_2, y_2, z_2) are the center positions of the trailing and leading particles, respectively. Here, we focus on the dimensionless results using length normalization d (particle equivalent sphere diameter), $\sqrt{dg}$ for velocity normalization, and time normalization $\sqrt{d/g}$. Fig. 14 represents the comparison of kissing time among the 65 models. In this plot, the kissing time refers to the time when the two particles are in contact in the first DKT process. It can be observed that the order of the kissing time corresponding to the four orientations is as follows: orient #1 > orient #2 = orient #4 > orient #3. We divide the 17 particles into two groups: the low sphericity group of particle #1 - particle #8, and the high sphericity group of particle #9 - particle #17. In the state of orientation #1, a decrease in both the sphericity and roundness can prolong the drafting stage, which is shown by a larger kissing time in Fig. 14. This tendency is more distinct in the low sphericity group which means the sphericity plays a more important role in the DKT process as it reduces. When the particle pairs are in the state of orientation #3, the particle shape has a small or even negligible effect on the drafting stage. It indicates that orientation #3 is the stable orientation (major-axis perpendicular to the falling direction) (Ardekani et al., 2016). The following DKT results and discussion are focused on orientation #3 unless otherwise stated. Moreover, it can also be noticed in Fig. 14 that it takes less time for the particle pairs with higher roundness in all orientations to come into the kissing stage. This can be explained by the less resistance generated between the fluid and particles with higher roundness, which accelerates the transition from the drafting stage into the kissing stage.

Here, the effects of roundness and sphericity on the DKT process are studied separately with the state of orientation #3 which is the stable orientation in the DKT process. First, it is meaningful to compare the gap D_r of different particle pairs with orientation #3 in the same row, that is similar sphericity, as shown in Fig. 4. The results in Fig. 15 show that lower roundness shortens the kissing stage, which is shown by the length/duration of flat lines in Fig. 15. It means that the lower roundness of particles accelerates the happening of the tumbling stage and makes the separation of particle pairs faster. It is reasonable because lower roundness means higher angularity which is adverse to the clustering of particles. Lower roundness represents sharper edges and corners, which means when two particles are in contact, the contact forces/moments and their directions are more complicated than spherical particles. In general, sharper edges and corners impede the contact status of particles through the generated contact forces/moments. Moreover, when the fluid flows through particles with sharper edges and corners, the flow field will be more disturbed. An asymmetric and complicated fluid flow field will in turn promote the horizontal and rotational movements of particles during the particle sedimentation in a viscous fluid. Both the contact and hydrodynamic interactions accelerate the separation of particle pairs with lower roundness. When particle pairs escape from the fluid fields around the other particle, their motion is stable until they land on the bottom wall. This result indicates that the clustering in a suspension of higher angular particles would be smaller and more difficult than that of spherical particles. Similarly, the effect of sphericity on the DKT process (shown in Fig.16) is also studied by comparing the gap D_r of different particle pairs with orientation #3 in the same column as displayed in Fig. 4. The uncertain tendency in the kissing duration shown in Fig. 16 can be explained by the fact that the roundness in the same column as displayed in Fig. 4 is not the exact same value. On the whole, the curves demonstrated in Fig. 16 show that the sphericity has less effect on the contact duration compared to the roundness. The definition of sphericity, which is a measure of the degree to which a particle approximates the shape of a sphere, determines the phenomenon reflected in Fig. 16. When the broad side of the particle pairs is perpendicular to the fluid streamline, that is orientation #3, the movement of particle pairs is relatively stable and takes place mainly in the sedimentation direction. Furthermore, there are no sharper edges and corners causing the complicated contact interactions and turbulent flow fields, and therefore the sphericity has no obvious effect to promote or hinder the separation of the particle pairs. Moreover, the duration of the drafting stage is similar for all the particle pairs with orientation #3, which is in agreement with Fig. 14. In conclusion, a small effect is caused by sphericity and roundness on the drafting stage while lower roundness accelerates the separation of particle pairs in the state of orientation #3.

We now investigate the effect of roundness and sphericity on the vertical velocity v_z of the particle pairs, namely the leading particle and trailing particle. Similar to the comparison of gap D_r, only the vertical velocities v_z in the state of orientation #3 are compared. First, the velocity comparison of different particle pairs in the same row, as demonstrated in Fig. 4, is shown in Fig. 17. It can be noticed that the vertical velocity v_z of both the leading and trailing particles is smaller with lower roundness. Lower roundness means sharper particles which can cause more obstacles to the fluid flow, which can in turn impede the movement of particle pairs, that is there is more resistance generated between the fluid and particles. Moreover, the asymmetric and complicated fluid flow fields around the particles with lower roundness contribute to the horizontal and rotational movements of the particle pairs, which takes away part of the vertical kinetic energy. Therefore, it is understandable that the lower roundness causes the lower vertical velocity v_z of both the leading and trailing particles due to the energy dissipation during interacting with the ambient viscous fluid and the energy dispersion into horizontal and rotational movements. The effect of sphericity is also studied in Fig. 18, which shows the velocity comparison of different particle pairs in the same column as illustrated in Fig. 4. The results in Fig. 18 indicate increasing the sphericity enhances the vertical velocity v_z of both the leading and trailing particles. Fig. 18 only compares the vertical velocity of particle pairs in the state of orientation #3, which means that the broad side of the particle pairs is perpendicular to the fluid streamline. In this study, the lower the particle sphericity is, the broader the particle side is perpendicular to the fluid streamline, which means there is a bigger obstacle to the fluid flow when the fluid bypasses the broader particle side. By action and reaction, the ambient viscous fluid will generate a bigger obstacle to the particle sedimentation with the broader side. Therefore, it is explainable that the particle pairs with higher sphericity drop faster in the vertical direction because the ambient viscous fluid creates a smaller obstacle to the particle sedimentation when its side perpendicular to the fluid streamline is narrower.

4. Conclusions

We have investigated the particle morphology effect on the DKT process by a coupled CFD-iDEM method. To do so, we first validated the CFD-iDEM method by two cases: flow over a fixed sphere with different Reynolds numbers and settlement of one particle with different fluid cell densities. Moreover, based on the studies of Ardekani et al. (2016), we simulated the settlement of oblate particle pairs to verify the points that the settling spheroids can resist horizontal motion by adjusting the particle's orientation to keep their broad side perpendicular to the fluid streamline direction. Then, the sedimentation simulations of 65 particle pairs under gravity were conducted to investigate the morphology effect: 16 irregular particles with four orientations and one spherical particle. We drew the following conclusions and observations from the conducted simulations:

1. When it comes to the orientation effect, the kissing time (the time that the particle pairs are in contact for the first time) follows this order: orient #1 > orient #2 = orient #4 > orient #3. It is easiest for the particle pairs, especially for the lower sphericity, in the state of orientation #3 to come into the kissing stage because their broad side is already perpendicular to the fluid streamline direction. Higher roundness shortens the drafting stage for all orientations due to less resistance generated between the fluid and particles.
2. The difference caused by orientations in the complete DKT process shows that it is gradually decreasing with the increase in particle sphericity. The DKT process was the most stable and similar for all the particle pairs with orientation #3. More complexity in the DKT process with lower sphericity corresponding to orientation #1 than that of orientation #3 can be explained by the fact that low sphericity particles tend to adjust their orientation so that their broad side keeps perpendicular to the fluid streamline direction.
3. By investigating the effect of sphericity and roundness on the DKT process separately with orientation #3, it can be observed that a negligible effect is caused by sphericity and roundness on the drafting stage while lower roundness accelerates the happening of the tumbling stage and makes the separation of particle pairs faster due to lower roundness hindering the clustering of particles.
4. By studying the effect of sphericity and roundness on the vertical velocity v_z separately with orientation #3, the vertical velocity v_z of both the leading and trailing particles is increased with higher roundness or sphericity. This can be explained by the fact that less resistance is generated between the fluid and particles with higher roundness, and the particle pairs with higher sphericity drop faster in the vertical direction because the ambient viscous fluid creates a smaller obstacle to the particle sedimentation when its side perpendicular to the fluid streamline is narrower.

Along with the particle shape, the particle size, density difference, and fluid viscosity are also significant factors controlling the DKT process. In the future, we will conduct a more comprehensive investigation on the factors affecting the DKT process, such as particle size, and density difference for particles with different morphologies.

CRediT authorship contribution statement

Xiaoming Zhang: Simulation and contributing to the writing of the first draft of the paper. **Pejman Tahmasebi:** Conceptualization, supervision of the project, writing the final draft of the paper, and funding acquisition.

Declaration of Competing Interest

The authors declare that they have no known competing financial interests or personal relationships that could have appeared to influence the work reported in this paper.

Data availability

Data will be made available on request.

Acknowledgments

This study was partially supported by NSF (Grant #CMMI-2000966), and NIH (Grant # P20GM103432).

References

Anthony, J.L., Marone, C., 2005. Influence of particle characteristics on granular friction. J. Geophys. Res. 110, B08409. https://doi.org/10.1029/2004JB003399.

Apte, S.V., Martin, M., Patankar, N.A., 2009. A numerical method for fully resolved simulation (FRS) of rigid particle-flow interactions in complex flows. J. Comput. Phys. 228, 2712–2738. https://doi.org/10.1016/j.jcp.2008.11.034.

Ardekani, M.N., Costa, P., Breugem, W.P., Brandt, L., 2016. Numerical study of the sedimentation of spheroidal particles. Int. J. Multiph. Flow 87, 16–34. https://doi.org/10.1016/j.ijmultiphaseflow.2016.08.005.

Azéma, E., Estrada, N., Radjaï, F., 2012. Nonlinear effects of particle shape angularity in sheared granular media. Phys. Rev. E 86, 41301. https://doi.org/10.1103/PhysRevE.86.041301.

Cho, G.-C., Dodds, J., Santamarina, J.C., 2006. Particle Shape Effects on Packing Density, Stiffness, and Strength: Natural and Crushed Sands. J. Geotech. Geoenvironmental Eng. 132, 591–602. https://doi.org/10.1061/(asce)1090-0241(2006)132:5(591).

Cleary, P.W., 2000. DEM simulation of industrial particle flows: case studies of dragline excavators, mixing in tumblers and centrifugal mills. Powder Technol 109, 83–104.

Clift, R., Grace, J., Weber, M., 1978. Bubbles, Drops, and Particles, Bubbles. Drops and Particles.

Cundall, P.A., Strack, O.D.L., 1979. A discrete numerical model for granular assemblies. Géotechnique 29, 47–65. https://doi.org/10.1680/geot.1979.29.1.47.

Dash, S.M., Lee, T.S., 2015. Two spheres sedimentation dynamics in a viscous liquid column. Comput. Fluids 123, 218–234. https://doi.org/10.1016/j.compfluid.2015.10.003.

Evans, D.J., Murad, S., 2006. Singularity free algorithm for molecular dynamics simulation of rigid polyatomics. 34, 327–331. https://doi.org/10.1080/00268977700101761.

Davydzenka, T., Fagbemi, S., Tahmasebi, P., 2020a. Wettability control on deformation: Coupled multiphase fluid and granular systems. Phys. Rev. E 102, 013301. https://doi.org/10.1103/PhysRevE.102.013301.

Davydzenka, T., Fagbemi, S., Tahmasebi, P., 2020b. Coupled fine-scale modeling of the wettability effects: Deformation and fracturing. Phys. Fluids 32, 083308. https://doi.org/10.1063/5.0018455.

Fortes, A.F., Joseph, D.D., Lundgren, T.S., 1987. Nonlinear mechanics of fluidization of beds of spherical particles. J. Fluid Mech. 177, 467–483. https://doi.org/10.1017/S0022112087001046.

Fries, L., Antonyuk, S., Heinrich, S., Palzer, S., 2011. DEM–CFD modeling of a fluidized bed spray granulator. Chem. Eng. Sci. 66, 2340–2355. https://doi.org/10.1016/j.ces.2011.02.038.

Ghosh, S., Kumar, M., 2020. Study of drafting, kissing and tumbling process of two particles with different sizes and densities using immersed boundary method in a confined medium. Appl. Math. Comput. 386, 125411 https://doi.org/10.1016/j.amc.2020.125411.

Glowinski, R., Pan, T.W., Hesla, T.I., Joseph, D.D., 1999. A distributed Lagrange multiplier/fictitious domain method for particulate flows. Int. J. Multiph. Flow 25, 755–794. https://doi.org/10.1016/S0301-9322(98)00048-2.

Goldstein, Herbert;, Poole, C.P., Safko, J.L., 2001. Classical Mechanics, 3rd ed. Addison-Wesley.

Hager, A., 2014. CFD-DEM on Multiple Scales - An Extensive Investigation of Particle-Fluid Interactions.

Hu, H.H., Joseph, D.D., Crochet, M.J., 1992. Direct simulation of fluid particle motions. Theor. Comput. Fluid Dyn. 3, 285–306. https://doi.org/10.1007/BF00717645.

Katz, O., Morgan, J.K., Aharonov, E., Dugan, B., 2014. Controls on the size and geometry of landslides: Insights from discrete element numerical simulations. Geomorphology 220, 104–113. https://doi.org/10.1016/j.geomorph.2014.05.021.

Kawamoto, R., Andò, E., Viggiani, G., Andrade, J.E., 2016. Level set discrete element method for three-dimensional computations with triaxial case study. J. Mech. Phys. Solids 91, 1–13. https://doi.org/10.1016/j.jmps.2016.02.021.

Krumbein, W.C., 1941. Measurement and geological significance of shape and roundness of sedimentary particles. J. Sediment. Res. 11, 64–72. https://doi.org/10.1306/D42690F3-2B26-11D7-8648000102C1865D.

Li, J., Langston, P.A., Webb, C., Dyakowski, T., 2004. Flow of sphero-disc particles in rectangular hoppers—a DEM and experimental comparison in 3D. Chem. Eng. Sci. 59, 5917–5929. https://doi.org/10.1016/j.ces.2004.07.022.

Lim, K.-W., Andrade, J.E., 2014. Granular element method for three-dimensional discrete element calculations. Int. J. Numer. Anal. Methods Geomech. 38, 167–188. https://doi.org/10.1002/nag.2203.

Lomholt, S., Stenum, B., Maxey, M.R., 2002. Experimental verification of the force coupling method for particulate flows. Int. J. Multiph. Flow 28, 225–246. https://doi.org/10.1016/S0301-9322(01)00045-3.

Marella, S., Krishnan, S., Liu, H., Udaykumar, H.S., 2005. Sharp interface Cartesian grid method I: An easily implemented technique for 3D moving boundary computations. J. Comput. Phys. 210, 1–31. https://doi.org/10.1016/j.jcp.2005.03.031.

Mittal, R., Dong, H., Bozkurttas, M., Najjar, F.M., Vargas, A., von Loebbecke, A., 2008. A versatile sharp interface immersed boundary method for incompressible flows with complex boundaries. J. Comput. Phys. 227, 4825–4852. https://doi.org/10.1016/j.jcp.2008.01.028.

Patankar, N.A., Singh, P., Joseph, D.D., Glowinski, R., Pan, T.-W., 2000. A new formulation of the distributed Lagrange multiplier/fictitious domain method for particulate flows. Int. J. Multiph. Flow 26, 1509–1524. https://doi.org/10.1016/S0301-9322(99)00100-7.

Powers, M.C., 1953. A new roundness scale for sedimentary particles. J. Sediment. Res. 23, 117–119. https://doi.org/10.1306/D4269567-2B26-11D7-8648000102C1865D.

Qi, D., 1999. Lattice-Boltzmann simulations of particles in non-zero-Reynolds-number flows. J. Fluid Mech. 385, 41–62. https://doi.org/10.1017/S0022112099004401.

Ritz, J.B., Caltagirone, J.P., 1999. A numerical continuous model for the hydrodynamics of fluid particle systems. Int. J. Numer. Methods Fluids 30, 1067–1090. https://doi.org/10.1002/(SICI)1097-0363(19990830)30:8. <1067::AID-FLD881>3.0.CO;2-6.

Robinson, D.A., Friedman, S.P., 2002. Observations of the effects of particle shape and particle size distribution on avalanching of granular media. Phys. A Stat. Mech. its Appl. 311, 97–110. https://doi.org/10.1016/S0378-4371(02)00815-4.

Seyed-Ahmadi, A., Wachs, A., 2021. Sedimentation of inertial monodisperse suspensions of cubes and spheres. Phys. Rev. Fluids 6, 44306. https://doi.org/10.1103/PhysRevFluids.6.044306.

Shinohara, K., Oida, M., Golman, B., 2000. Effect of particle shape on angle of internal friction by triaxial compression test. Powder Technol 107, 131–136. https://doi.org/10.1016/S0032-5910(99)00179-5.

Shirgaonkar, A.A., MacIver, M.A., Patankar, N.A., 2009. A new mathematical formulation and fast algorithm for fully resolved simulation of self-propulsion. J. Comput. Phys. 228, 2366–2390. https://doi.org/10.1016/j.jcp.2008.12.006.

Tahmasebi, P., Kamrava, S., 2019. A pore-scale mathematical modeling of fluid-particle interactions: Thermo-hydro-mechanical coupling. Int. J. Greenh. Gas Control. 83, 245–255. https://doi.org/10.1016/j.ijggc.2018.12.014.

Ten Cate, A., Nieuwstad, C.H., Derksen, J.J., Van den Akker, H.E.A., 2002. Particle imaging velocimetry experiments and lattice-Boltzmann simulations on a single sphere settling under gravity. Phys. Fluids 14, 4012–4025. https://doi.org/10.1063/1.1512918.

Wadell, H., 1932. Volume, Shape, and Roundness of Rock Particles. J. Geol. 40, 443–451. https://doi.org/10.1086/623964.

Walton, O.R., Braun, R.L., 1993. Simulation of rotary-drum and repose tests for frictional spheres and rigid sphere clusters.

Wang, L., Guo, Z.L., Mi, J.C., 2014. Drafting, kissing and tumbling process of two particles with different sizes. Comput. Fluids 96, 20–34. https://doi.org/10.1016/j.compfluid.2014.03.005.

Xue-ming, S., Yang, L., Zhao-sheng, Y., 2005. Interactions between two sedimenting particles with different sizes. Appl. Math. Mech. 26, 407–414. https://doi.org/10.1007/BF02440092.

Yu, Z., Shao, X., Wachs, A., 2006. A fictitious domain method for particulate flows with heat transfer. J. Comput. Phys. 217, 424–452. https://doi.org/10.1016/j.jcp.2006.01.016.

Zhang, X., Tahmasebi, P., 2022a. Coupling irregular particles and fluid: Complex dynamics of granular flows. Comput. Geotech. 143, 104624 https://doi.org/10.1016/j.compgeo.2021.104624.

Zhang, X., Tahmasebi, P., 2022b. Investigation of particle shape and ambient fluid on sandpiles using a coupled micro-geomechanical model. Powder Technol 117711. https://doi.org/10.1016/j.powtec.2022.117711.

Zhang, X., Tahmasebi, P., 2019. Effects of Grain Size on Deformation in Porous Media. Transp. Porous Media 129, 321–341. https://doi.org/10.1007/s11242-019-01291-1.

Zhang, X., Tahmasebi, P., 2018. Micromechanical evaluation of rock and fluid interactions. Int. J. Greenh. Gas Control 76, 266–277. https://doi.org/10.1016/J.IJGGC.2018.07.018.

Zhu, H.P., Zhou, Z.Y., Yang, R.Y., Yu, A.B., 2008. Discrete particle simulation of particulate systems: A review of major applications and findings. Chem. Eng. Sci. 63, 5728–5770. https://doi.org/10.1016/J.CES.2008.08.006.

Zhu, H.P., Zhou, Z.Y., Yang, R.Y., Yu, A.B., 2007. Discrete particle simulation of particulate systems: Theoretical developments. Chem. Eng. Sci. 62, 3378–3396.